LATVIAN
JOURNAL
of
PHYSICS
and TECHNICAL
SCIENCES

ISSN 0868 - 8257

1

(Vol. 61)

2024

CONTENTS

LATVIAN
JOURNAL
of
PHYSICS
and TECHNICAL
SCIENCES

LATVIJAS
FIZIKAS
un TEHNISKO
ZINĀTŅU
ŽURNĀLS

Published six times a year since February 1964
Iznāk sešas reizes gadā kopš 1964. gada februāra

1 (Vol. 61) • 2024

RĪGA

Language Editor: O. Ivanova
Computer Designer: I. Begicevs

INDEXED (PUBLISHED) IN

www.scopus.com
www.sciendo.com
EBSCO (Academic Search Complete, www.epnet.com), INSPEC (www.iee.org.com).
VINITI (www.viniti.ru), Begell House Inc/ (EDC, www.edata-center.com).

Issuers: Institute of Physical Energetics,
Institute of Solid State Physics, University of Latvia
Registration Certificate Number: 000700221

Editorial Contacts:
14 Dzerbenes Street, Riga, LV-1006
LATVIA
tel: +371 26245896
M: +371 29363105
leo@lza.lv

THE 60th ANNIVERSARY OF THE LATVIAN JOURNAL OF PHYSICS AND TECHNICAL SCIENCES

2024 is a remarkable year for both the editorial team and the readers and authors of the Latvian Journal of Physics and Technical Sciences – it marks the 60th anniversary of the journal's publication history, which started in February 1964 with Issue One of "Proceedings of the Academy of Sciences, the Latvian Soviet Socialist Republic. Series of Physics and Technical Sciences". In its introduction, the Editors wrote, "A new scientific journal is published—a separate series dedicated to physics and technical sciences." The first issue of the journal included the works of prominent and renowned scientists such as I. Kirko, J. Lielpeteris, J. Mihailovs and many others.

The new journal emerged in the field of physics and technology, as the volumes of scientific and research work grew so rapidly that the journal "Proceedings of the Latvian Academy of Sciences, the Latvian Soviet Socialist Republic" alone was no longer able to ensure timely publication of scientific articles in technical fields. A. Malmeistars was the organizer and first editor of the journal, and it was decided that the journal would have the following thematic coverage: physics, astrophysics, mathematics, cybernetics, mechanics, automation, electronics and energy.

Over time, the journal's coverage areas changed due to the creation of new journals at the Academy of Sciences of the Latvian Soviet Socialist Republic ("Magnetic Hydromechanics of Liquid Metals" and "Composite Mechanics" in 1965, etc.). The number of publication proposals increased from year to year, covering new and important areas of scientific research both in Latvia and worldwide. At that time, the journal was published only in Russian.

Throughout the period of 60 years, the Editors-in-Chief of the journal were A. Malmeistars (1964–1965), J. Mihailovs (1965–1967), V. Apsitis (1968–1981), A. Krogeris (1981–1989), J. Ekmanis (1990–2016), I. Oleinikova (2016–2018), and N. Zeltins (2018–onwards).

Since 1991, the journal has been known as the Latvian Journal of Physics and Technical Sciences (LJPTS), with articles initially published in three languages: Latvian, English and Russian. The first editorial team of LJPTS consisted of J. Ekmanis (Editor-in-Chief), V. Gluchovs, I. Bersons, I. Feltina, V. Greislis, I. Iljina, E. Klotins, Z. Krisans, E. Sukhovich, K. Schwartz, U. Ulmanis, and S. Ezerniece (Managing Editor). A special tribute should be paid to S. Ezerniece, who served as the Managing Editor of the journal from 1964 until the end of 2019. During this time, several generations of scientists have worked in the journal, and S. Ezerniece has become a legend in preparing and disseminating the results of several hundred world-class scientific research projects.

In the years to come, the composition of the editorial teams changed, including not only the scientists from Latvia (A. Ozols, V. Zebergs, J. Yolins, Z. Krishans, A. Silins and others), but also from other countries: in 2002, J. Willem (Lithuania) became a member of the Editorial board, followed by J. Kapala (Poland), J. Blacktail (the USA), and T. Jaaskelainen, (Finland).

The important turning point in the history of LJPTS came in 2018, when on

13 November, a cooperation agreement was signed between the Institute of Physical Energetics and the Institute of Solid Physics of the University of Latvia regarding the publication of the journal. The parties agreed to cooperate in the preparation, publication and financing of LJPTS as its co-owners and co-publishers.

The new editorial board was then created, including N. Zeltins (Editor-in-Chief), A. Sternbergs (Deputy Editor-in-Chief), E. Birks, J. Kalnacs, G. Klavs, A. Kuzmins, A. Mutule, A. Ozols, L. Ribickis, M. Rutkis, A. Silins, A. Sarakovskis, L. Jansons (Managing Editor, since 2019). The newly created Advisory Board included J. Vilemas (Lithuania), L. Gawlik (Poland), J. Melngailis (USA), T. Jaaskelainen (Finland), M. Balodis (Latvia), and A. Udalcovs (Sweden).

This turning point marked a new era in the journal's history, becoming a truly European-scale scientific publication platform with much to offer. Furthermore, since 2008, the journal has been published only in English and is exclusively available in electronic format. The main thematic coverage of the journal is now dedicated to several areas in and around energy and materials science subjects, as well as astronomy and physical science.

Through cooperation with the Sciendo platform – a leading provider of publishing solutions for academic journals, books and conference proceedings, and as a member of De Gruyter publishing group –, LJPTS has reached many remarkable achievements. Today, the journal is indexed in numerous databases, including Scopus and Web of Science.

All the information regarding the journal and its current publishing activities, metrics and other important facts is available online:
https://sciendo.com/journal/LPTS.

Editorial board

sciendo

LATVIAN JOURNAL OF PHYSICS
AND TECHNICAL SCIENCES
2024, N 1

DOI: 10.2478/lpts-2024-0001

HIGH RESOLUTION QUADRUPOLE MASS SPECTROMETER FOR ION BEAM PROCESSING

J. Blahins*, A. Bzhishkian

Institute of Atomic Physics and Spectroscopy,
University of Latvia,
19 Rainis Blvd., Riga, LV-1586, LATVIA
FOTONIKA-LV,
4 Šķūņu Str., Riga, LV-1050, LATVIA
*e-mail: janis.blahins@lu.lv

The mass filtering equipment in the ion beam processing industry plays a vital role. Mass filtering is usually achieved through classic magnetic mass selector techniques. The drawbacks of these techniques are the dimensions, weight, price, and power consumption. We suggest mitigating it by using the electrostatic RF mass selector instead of the magnetic one. We discuss the development of a novel ion beam processing apparatus that employs a QMS filter in a vacuum of superior purity. We describe the experimental setup in terms of part design. The article presents the successful test results of that parts. The article also explains in detail the basic principles and the technical realization of the whole apparatus and presents experimental data showing its high capabilities.

Keywords: *Boron ion beam, implantation, quadrupole mass selection.*

1. INTRODUCTION

For most ion beam technologies, especially for ion implantation, the due beam purity is needed, so it is attained by some kind of a mass filter. Historically, for this aim filtering by the magnetic field was used. In the last decade, it was possible to see the technical benefits of engineering the mass filter employing electrostatics, namelyz, quadrupole mass selector (QMS). Radio-frequency (RF) QMS may give a boost of selectivity up to the single isotopic level if desired; it consumes far less electricity than magnetic selectors, and is much less weighty, smaller, and cheaper. For laboratory-created physical instruments, QMS dimensions allow choosing between a classical inox vacuum chamber or – in the best case – half of order cleaner and significantly simpler to produce silica-glass vacuum vesicles. Today most factory-made QMS has understood the analytical instrument of high cost, however, quadrupole principle offers a much broader technological use. We demonstrate that mounting the QMS rods into the beam-line technological instruments is well beneficial and possible even by moderate-high level scientific personnel.

It is worth mentioning that about 70 % of implantation market revenue worldwide is produced by small innovative R&D firms; thus, the segment of 1.5–3 billion USD in size has a "vacuum" of corresponding cheap and easy to re-arrange table-size machinery for small firms [1]. The offered QMS technology may become a key to design a small, customizable, non-expensive implantation adapted to small-firms' "easy to re-adapt" wishes.

The current situation in the industry: Mostly ion beam sources operate with high-purity beams, which at an extreme may demand so high purity as 1: 10^20. Thus, an ion beam instrument has to have some sort of good mass filter into the beam line. It is known that the magnetic field has a much stronger impact on the acceleration than the electric field (for orientation, 1 Tesla is roughly equivalent to 300 kV/mm). Therefore, historically, the magnetic mass filter principle was used, later spreading into numerous sub-varieties, such as configurations of Bainbridge-Jordan, Mattauch-Herzog, Hinterberger-Konig, Takeshita, Matsuda, Nier-Johnson and more as explained in [2].

Although magnetic filters are highly popular and trusted, they have drawbacks as well – large, heavy, expensive and energy inefficient. Anyway, until now there were not many choices. Contrary to electric field-based filters widely used in analytical chemistry, the QMS filter devices are better with the highest possible performance (resolution), sorting devices may be of different dimensions – from 50 mm in diameter and 25 cm long to a few millimetres. QMS is energy efficient and mechanically minimalistic with a rod price expected around 4 K$ for the advanced model. It was believed for a long time that ionic transparency of the QMS tract was too weak for use in beamlines. Ion beam is the ratio between the output flux of well-adjusted mole-mass particles and input flux, similar to optics transparency, which is brightness in output divided by input. Overall producers' list of such rod assemblies is short, from Shimadzu and Morgan to Reliance. Even large analytical QMS apparatus producers, such as Pfeiffer, Varian, and others, purchase rod assemblies as outsourced [3] product [4], [5].

To illustrate the topicality of ion beam purification change in the industry, especially in the ion implantation industry, from magnetic filters towards QMS, some studies [6], [7] should be highlighted. The appropriateness of QMS over the magnetic mass filters was explored by [8]. The QMS-based filtering approach in a broad perspective was discussed in the recent PhD Thesis [9]. However, for larger ion flux obstacles (mean larger ion current) the QMS construction ought to have some differences from the purely analytical constructions, the QMS principle still allows us to get good results, according to [10]. This is also the reason why CERN implemented QMS in the modernization of the ion ring ISOLDE instead of the classical magnetic mass filter system [11]. This means that "scientific fashion" is already turning towards QMS instead of magnetic separators, and it gives numerous benefits.

Thus, the instrument basics is an assembly having four (or more rarely six) ultra-precision rods assembly, made of the best available material – pure molybdenum. However, poor-man constructions may be machined out of stainless steel. Rods are fixed in two or three ceramic keeper rings, which position this assembly against the vacuum chamber walls. Between the rods, the superposition of DC and RF AC voltages is applied, whose ratio determines the molar mass onto which the mass filter is adjusted to be transparent. All non-adjusted mole-mass ions hit the rods' side surfaces and, thus, are evacuated by the vacuum pump. All the re-adjusting of mass is made by adjusting electronics alone, being just the voltage ratio. For decades, such a highly accurate electronic generator was something rather complicated. However, for already a decade or two there are numerous trade models of cheap and good, crystal stabilized digitally synthesized generators (stability at least 1:10^12 or better depending only on the crystal) called DDS available on the market. Its output power demands a surplus amplifier to get the proper resolution factor.

The next practical question is about the vacuum tract. For beamline to work in a vacuum, mostly the chamber form factor is pipe-like construction made of AISI-306-316 or at high-purity instruments – pure metallic molybdenum. Thus, the costs of steel works may account for more than half of the project funding. We tried to elaborate on the cheaper highest purity system concept that is easy to implement. Learning from past century vacuum technologies, the glass pipes were then well suited for vacuum systems. However, glass may not maintain as good as 1E-9 Torr or at least 1E-7, being the kind of standard for high-energy ion beams. Such purity, contrary, may be sustained by the quartz, or more precisely in terminological terms – high purity silica-glass, because scrupulously speaking, quartz always stays in the crystalline form, while only non-crystalline quartz is weldable and blowable with the propane-oxygen torch. Silica glass called Ultrasil is a weldable material; however, the glassblower man hand must be trained-up well. When the silica-glass pipe is hot-formed according to demanded sizes, there must be laid thrue the wall numerous electrodes. There are two alternatives available. Firstly, silica glass is weldable together with the so-called molybdenum glass. Molybdenum glass is well wetting the molybdenum metal surface, thus making the well-hermetic joint between metal and glass. Secondly, there are high-vacuum compatible epoxy resins that may fix the wire metal inside the side-tubules. We spent time elaborating on the best method to drill in the thick quartz wall the cone-shaped hole in the size of a wire, giving a better hermetical joint around the wire and found an un-traditional solution in the nail beauty industry - where a specialized diamond powder cone-shaped micro drills are mass-made product.

After the vacuum tract is welded, it must be baked in the oven to release the tensions, despite the thermal expansion being so low as 5.5E-7/ °C between 20–320 °C – when metals have stainless (1.01–1.73) E-5 or ordinary steel (1.1–1.3)E-5 [12]. The best method to check the quality of baking is to put the part between two polarization filters (even photographic quality is suited enough) and adjust it to the most black position. Each tension patch will be well observable to the naked eye. Silica-glass has one more advancement over metal vesicles, i.e., simplicity of processing at a lower level equipped workplace. Specifically, it is capable of maintaining half of the order cleaner vacuum environment over molybdenum or more in comparison with the stainless environment, yet stipulating that proper surface cleaning is provided. Basically, among three vacuum pollution constituents, the largest one is made by the surface-sorbed monomolecular layer of gases. It grows very fast but detaches very slowly. The routine solution is to warm up the surface as high as practically possible (100 °C water, 200–300 °C oil bath, or the resistor bandage), and when the pressure increase slows down, then it is necessary to switch from warming to sharp cooling (4 °C of water or minus 196 °C for LN2). Anyway, de-gassing is an energy demanding and slow process to get a good vacuum in the system. Then one second of the door being opened is required and all must be repeated anew. Our receipt: For the silica-glass case, this routine may be changed, giving an obvious win. The surface out-gassing of Ultrasil is one order of magnitude over the best metals normally (most table readers miss to hear the next most important): half-order less of it after etching. Thus, without etching the result will be not so good, but with etching, the result will be the best of the best [13]. The first step is to substitute the air monomolecular layer on the surface with an inert gas layer. Therefore, we use the argon gas flowing through in a dynamic vacuum regime and when the vacuum is at least 10^-5 up to -6 we apply etching.

Technically, electrical etching may be made by two methods: a) It may be processed by DC HV or 50 Hz AC HV plasma discharge (about 200 kOhm 50 W and 3 kV). The source of voltage ideally suited is MOT taken off the microwave cooking device. b) The better etchant is ICP plasma – about 1...3 kV and 1–10 A in the resonant tank of 27.13 or 40.6 up to 50.4 MHz (harmonics of 13.56 MHz making no interference with radio and TV). The electrode then must not be mandatory inserted inside the vacuum glass pipe as it is demanded in metallic chambers. It is also possible to use a serial tank at 20– 30 V and 5–10 A with MOSFET (Clapp circuit or e-class Pierce circuit, best results attained with vertical channel devices). Thus, the voltage is built up by a resonant tank Q-factor, or on the contrary, a parallel tank at 1–3 kV may be used and fed by a pair of vacuum triodes 50–100 mA (Royer circuit), and the current is built up by a resonant tank Q-factor. The last but not least issue is how to practically get the ICP coil over a glass pipe. To resolve the issue, there is an open-configuration coil (see Fig. 1), which may easily be hung and slide along the pipe surface, thus implementing the degassing (etching) process.

Fig. 1. Open type coil for etching.

The first confusion in the most popular pictures of how to connect QMS to voltage sources is the placement of GND that looks like QMS has no GND wire [14] (Fig. 6.5 in the reference). However, the ground may not be absent to work properly, GND is the conductor layer wrapped around the QMS rods assembly inside the quartz pipe, or the vacuum chamber walls if metallic. Wrapping the foil outside will not work because of charge buildup on the inner quartz wall.

Another technical issue is the superposition of DC with RF voltage, which many authors draw like the two transformers winding. Thus, the V+U and V-U come at output just naturally. The 2 kW transformer core at 3 MHz may cause some difficulties; however, the well-passed ferrite trademark solves it well. The strong lure is to combine the source by two DC identical sources with the floating ground and one RF generator, but such a strategy ends anyway in the RF transformer because of GND point necessity. At first, we decided to use the modern-day DDS generator ready-made circuitry. However, after obtaining and checking several trademarks the decision is that they are far too inaccurate about signal form purity, except for the very low frequencies. However, digital generator theoretically may feed the QMS by the meander signal instead of sinusoidal, but the filtering purity with such will sharply decrease and in the case of many harmonics (what is the case at DDS), the situation becomes worse. Therefore, the sinusoidal shape must be more than good, as noted in [15]. Thus, the frequency was given by an ARM computer clock, but the right signal form was obtained by a resonant tank, filtering out all harmonics. The required frequency stability and accessibility to adjust frequency by computer were obtained by such a design. The lost ability for broad frequency sweep so important for analytical chemistry here is completely unneeded because our frequency is never changed. For DC we designed optically isolated half-bridge SMPS on the basis of TL594, which is of high precision relative to popular TL494. Link to the computer to adjust the voltage is made by a local ARM processor translating signals between the table computer and multiple power supplies via the LAN cable.

Experiments on QMS: The most crucial question is: Do our QMS is transparent enough? If accuracy is high enough, then transparency ought to be good [16]. We used 0.25 micron accurate assembly, according to the datasheet of the producer. A good aid to realise how to manage calculations is the PhD Thesis [17]. Putting the Faraday Cup before QMS and later repositioning the FC after the QMS we obtained that >90 % of ions of adjusted mass going through it were not lost. On the contrary, detuning QMS adjustments off the boron that we used for target mole mass, the FC current diminished more than 100-fold, i.e., the filtering factor was at least 100. However, this last measurement was struggling with white noise, so the figure should not be very accurate. The calculated filtering factor was 150-fold. By the way, many popular books and articles show how to obtain the QMS U and V to adjust the target mass. Less attention is devoted to how to use not only the first stability isle but also the second and even the third [6].

A few studies examine how the choice affects the filtering factor and even fewer studies investigate how to find the demanded RF power consumption. At least at the Pfeiffer homepage, we found the formula N=C/Q*M^2*f^5*ro^4, yet giving by orders of magnitude confusing Petawatt scale result [14] (formula 6.11 in the reference). After mailing to Pfaiffer with questions we got a kind reference to an original historical publication [18], stating that N=6.5E-4*(C/Q)*M^2*f^2*ro^4 (W; pF; MHz; cm). However, a mistake at the homepage was not corrected. However, we dared to elaborate our own methodology to assume this value and it gave us another choice to rely on. Generally, the better one wants the filtering factor, the larger must be the voltages, and by them in a square, the larger power of RF. Our method was such: firstly, it is necessary to calculate or measure the QMS rod assembly capacitance. We did it and the calculated value fell in the range of ±50 % measured to calculated (!). Probably, the reason was large fringent field loss. Measurement of so small capacitance was made by Nano-VNA-v2.0. Then assuming no large impact of power-line and amplifier impedance, the reactance X(c) is in resonance with RF transformer winding, thus the loss is dependent on filter quality factor Q. For electronic engineers, the default Q of QMS sounds surprising, within an order of a million, but so is suggested in the literature about QMS. Then Nloss=V^2/Rloss, where R is taken from Q=2*pi()*f*Rparal*C resulting in Nloss=V^2/2/pi()/f/Q/C. Here the second formula gives 4 milliwatts and the last gives 2 Watts at 1 MHz or 19 W and 0.11 W at 3 MHz. Our goal was 3 MHz demanding 309 V RF and 58 V DC for boron. From the standpoint of circuit design for 0.1 W and 20 W there is no big difference, we left the question temporarily unanswered, designed 20 W model and it works well.

4. RESULTS AND DISCUSSION

As a proof of concept, we connected the innovative boron ion source consisting of pure elemental boron in solid state form. The Hollow Cathode discharge was maintained. The incoming argon carrier gas was excited using an ICP coil so that the boron insert received heat. At HC output, straight after the HC anode short pipe, another ICP exciter coil was applied, which altered the ions to neutral atom ratio. Ions were extracted by an extractor cone with a 167 deg angle between sidewalls, looking with the smallest diameter toward the ion source. After the extractor in the beamline is placed temporary Faraday cup, measuring the ion beam current. After due data are collected, it is taken away. The system is used under dynamic vacuum – in the low vacuum section about 1 millitorr and in the high vacuum section better than 1 micro torr.

The second experiment setup was made to measure the QMS assembly transparency for boron as described above, but the Faraday cup was placed after QMS. The result was about 90 %. Yet it is difficult to guarantee that plasma after re-ignition is very identical each time by brightness in spite of the current being stabilized. Thus, we made a series of switch on and switch out cycles to access the uncertainty value. We believe that uncertainty of the transparency figure is about 5 %.

Another disturbing factor is the impurity content in boron. We used 99.5 % purity powder; thus, the 0.5 % deviation might be caused by this impact. Our QMS was the product of Reliance Ltd, with diameter of 12 mm and length of 18 cm. Finally, it is important to mention the size and weight of the device. Compared to the Wien velocity filter, we also experimented with a separation factor so woeful as 4 but weighting 7 kg and consuming 2–5 A at 5–15 V, thus, below 75 W (Colutron, model 300 [19]). QMS weights about 150 g except for the vacuum chamber, having a separation factor to be adjusted in a wide range according to the needs and wishes.

In this study, we examined five different cases of ventilation element, whose design was based on the concept of constant cross-sectional area. As discussed above, some elements may work well at lower air velocity but can be less efficient at higher velocities and vice versa. This is a crucial point to note because certain elements can operate very well at lower velocities but have poor performance at higher velocities, making it crucial to select the appropriate element in accordance with operating parameters. Moreover, results depict that flow energy losses decrease with a decreasing reference coordinate angle in design of elements from 90° to 30°, specifically at higher air velocities. This means that with a decreasing angle in the design of outer ring, the results improve gradually.

It can be concluded that element E1 provides better results both at lower and higher air velocities. Moreover, E1 has the smallest energy losses in the element flow channel and shows lower fluctuations in pressure and temperature difference with the change in air velocity than the other elements. This makes element E1 more suitable over the other elements, which could provide better cooling at different inlet air velocity. Although choosing the right design can be challenging, it can be done with careful optimization and simulation analysis. CAD design and CFD software can be very important tools for such a purpose as they save a lot of time and reduce costs of manufacturing and real life experiments. In addition, the created models can be used to compare ventilation efficiency analysis, enabling further studies, such as improving the position of various ventilation elements on protective garments.

5. CONCLUSION

We presented a novel ion beam purification apparatus concept with greater potential in ion implantation technologies, made of well-known parts traditionally used for other aims, but also appropriate in a wide range of ion beam technological apparatuses, where the ion beam purity is demanded.

The system is capable of filtering (cleaning) any charged ion beam, where adjusting on desired mass happens electrically. As a proof of concept, we demonstrated a series of experiments performed with DIY-created concept demonstration apparatus created in the frame of a specific ERDF Project quoted below.

ACKNOWLEDGEMENTS

The research has been financed by the EU ERDF Project ESS2020/381 - CFLA 1.1.1.1/19/A/144.

REFERENCES

1. Transparency Market Research (n.d.). *Ion Implantation Machine Market 2020. Overview.* Available at www.transparencymarketresearch.com/ion-implantation-machine-market.html
2. Burgoyne, W.B., & Hieftje G.M. (1996). An Introduction to Ion Optics for the Mass Spectrograph. *Mass Spectrometry Reviews, 15* (4), 241–259.
3. Reliance Precision. (2007). *Clean Assembly and Manufacturing Solutions for the Scientific, Medical and Analytical Industries.* Commercial Brochure. Available at www.reliance.co.uk/wp-content/uploads/2017/03/SPSI3-Scientific-Issue-B-web.pdf
4. Morgan Technical Ceramics. (n.d.). *Quadrupole Components.* Available at www.morgantechnicalceramics.com/en-gb/products/quadrupole-components/?gclid=EAIaIQobChMIp43-maOs9QIV0sLVCh2BwgFhEAMYASAAEgLBSvD_BwE
5. Shimadzu. (n.d.). Hardware: Mass Analyzer. Available at www.shimadzu.com/an/service-support/technical-support/analysis-basics/gcms/fundamentals/analyzer.html
6. Konenkov, N.V., Seregin, K.E., Makhmudov, M.N., & Konenkov, A.N. (2020). Stable X-Islands of Quadrupole Mass Filter. *European Journal of Mass Spectrometry*, *26* (1), 78–87. doi: 10.1177/1469066719856827.
7. Shagimuratov, G.I., Konenkov, N.V., Silakov, S.S., & Mogilchenko, G.A. (1990). Transmission and Resolution of a Quadrupole Mass Filter in the Intermediate Region of Stability of Separation Regime. *Zhurnal Tekhnicheskoj Fiziki*, *60* (1), 117–122.
8. Johnson, G.E., Hadjar, O., & Laskin, J. (2011). Characterization of the Ion Beam Focusing in a Mass Spectrometer Using an IonCCD™ Detector. *Journal of the American Society for Mass Spectrometry, 22*, 1388–1394.
9. Walz, A. (2020). *Compact and Versatile Electrospray – Controlled Ion Beam Deposition with Adjustable Frequency RF Ion Guides and Extended Mass Range.* PhD Thesis. Department of Physics, Technical University of Munich. Available at https://mediatum.ub.tum.de/doc/1575832/1575832.pdf.
10. Sleno, L., & Volmer, D.A. (2005). Tutorial – Mass Analyzers: An Overview of Several Designs and Their Applications, Part I. *Spectroscopy*, *20* (11). Available at: www.spectroscopyonline.com/view/tutorial-mass-analyzers-overview-several-designs-and-their-applications-part-i
11. Khidr, E. (2019). *Simulation of an Off-Line Ion Beam System at ISOLDE*. CERN publications. Available at https://cds.cern.ch/record/2687886/files/Summer_student_report_2019.pdf
12. Momentive. (n.d.). *Quartz Producer Homepage and Data*. Available at www.momentive.com/en-us/categories/quartz/thermal-properties
13. Chiggiato, P. (2017). Materials and Properties IV, Outgassing. *CERN Accelerator School on Vacuum for Particle Accelerators*. Available at https://indico.cern.ch/event/565314/contributions/2285743/attachments/1466415/2277367/Outgassing-CAS-Lund-final.pdf
14. Pfeiffer. (n.d.). *Educative Data on QMS.* Available at www.pfeiffer-vacuum.com/en/know-how/mass-spectrometers-and-residual-gas-analysis/quadrupole-mass-spectrometers-qms/quadrupole-mass-filter/
15. Voo, A.C.C., Ng, R., Tunstall, J.J., & Taylor, S. (1997). Transmission through the Quadrupole Mass Spectrometer Mass Filter: The Effect of Aperture and Harmonics. *J.Vac.Sci.Technol., 15* (4). Available at www.liverpool.ac.uk/media/livacuk/massspectrometry/pdfs/Transmission,through,the,quadrupole,mass,spectrometer,mass,filter,the,effect,of,aperture,and,harmonics.pdf
16. Taylor, S., & Gibson, J. (2008). Prediction of the Effects of Imperfect Construction of a QMS Filter. *Journal of Mass Spectrometry, 43*, 609–616.

17. Richards, J.E. (1972). *An Improved Quadrupole Mass Spectrometer*. South Wales University. Available at http://unsworks.unsw.edu.au/fapi/datastream/unsworks:57647
18. Balzers facktbericht. *Das Funktionsprincip des Quadrupol-Massenspektrometers.*
19. Beam Imaging Solutions. (n.d.) *Data of Colutron Parts.* Available at https://beamimaging.com/colutron-research-corporation/

LATVIAN JOURNAL OF PHYSICS
AND TECHNICAL SCIENCES
2024, N 1

DOI: 10.2478/lpts-2024-0002

EXPOSURE BUILDUP FACTORS IN CONCRETE, LEAD FOR POINT ISOTROPIC AND UNIDIRECTIONAL PHOTON SOURCES IN THE ENERGY RANGE FROM 10 TO 50 MeV

I. Alhagaish*, A. K. Aqili

Physics Department, Faculty of Science, Hashemite University,
P.O.Box 330127, Zarqa 13133, JORDAN
*e-mail: iyadk@hu.edu.jo

The exposure buildup factors in concrete and lead for a point isotropic and flat unidirectional photon source in the energy range from 10 to 50 MeV were determined using Monte Carlo simulation "FLUKA" software. The exposure buildup factors were also obtained for different material thickness up to 40 mpf. The calculations were done in a barrier geometry where the contributions of all photon-matter interactions were taken into account in the performed calculations. Amendments for the barrier-geometry effect for both materials under study were deduced. The results showed that barrier-effect amendments were independent of the material thickness, material type, and energy of the photon source

Keywords: *Bremsstrahlung, buildup factor, doses, electronic accelerators, isotropic, shielding.*

1. INTRODUCTION

The wide usage of linear electron accelerators (especially accelerators producing electron beam energy up to 50 MeV) in medicine and therapy increases the need to improve the radiation safety of personnel and the public. Such improvement requires the enhancement of the methodological basis for designing the shielding of such installations. A significant step in this direction is to obtain the attenuation properties of the shielding materials used in the radiation protection of these installations taking into account the scattered radiation [1]. One of these properties is the so-called buildup factor which can be calculated using advanced engineering methods by the calculation of the scattered radiations. The information available in the literature for photon buildup factors for various protective materials [2]–[4] is limited especially for a point isotropic monoenergetic photon source in the energy range from 10 to 50 MeV.

In this study, we performed calculations of the dose (absorbed dose rate in air) distributions of photons in barriers made of concrete and lead with a density of 2.3 and 11.3 g / cm^3[3], respectively, with thickness up to 30 mean free paths for a point isotropic source of monoenergetic photons with energy of 10, 20, 30, 40 and 50 MeV. The calculations were done using the Monte Carlo method FLUKA [5]. All types of "photons with matter" interactions and contributions of characteristic, annihilation, and bremsstrahlung radiation to the calculated dose were taken into account. The transition from the free path length (mfp) to the true distance in linear dimensions was performed using the mass attenuation coefficients of photons from the publications [2], [6].

2. METHODOLOGY

The geometries of the concrete and lead are identical and are shown in Fig. 1.

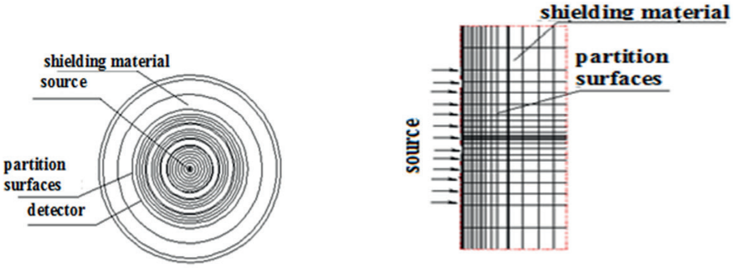

Fig. 1. Geometries of the considered compositions: a) – point source, b) – unidirectional source).

To examine the influence of the source geometry on the shielding properties of the concrete and lead, two cases were considered: (i) spherical geometry with a point isotropic source in the centre of the sphere and (ii) cylindrical geometry with a flat unidirectional source whose radiation falls normally on the end surface of the cylinder. In order to test the effect of barrier protection on shielding properties, calculations were performed selectively in the barrier geometry. The thickness of the materials was selected to be ranged from 0 to 30 mean free paths for the point source. The radius of the cylindrical shielding was 1000 cm for concrete and 300 cm for lead. The radius of the unidirectional source was assumed to be 300 cm for concrete shielding and 200 cm for lead shielding. To calculate the absorbed dose rate in air, the specific dose coefficients given in Table 2 were used and the following formula was utilized:

$$\delta = 10^5 \mathrm{E}_\gamma \ 1.6 \times 10^{-13} \mu_{\mathrm{em}}^{\mathrm{m}}(\mathrm{E}_\gamma), \ \ \mathrm{cGy}.\frac{\mathrm{cm}^2}{\mathrm{photon}}, \qquad (1)$$

where Eγ – the photon energy, in MeV;
$\mu_{\mathrm{em}}^{\mathrm{m}}(\mathrm{E}_\gamma)$ – a photon energy-absorption coefficient for air with energy Eγ; cm^2/g, 1.6×10^{-13} ; J/MeV – a transition coefficient from Joule to MeV.

The values of δ for photon energy less than 10 MeV were taken from [5], and large photon energies are calculated by means of Eq. (1) using $\mu_{\mathrm{em}}^{\mathrm{m}}$, (Eγ), taken from [6]. Moreover, the photon mass attenuation coefficients [2], [6] given in Table 1 were used for the transition from the mean free path to the true distance in linear dimensions.

Table 1. Photon Mass Attenuation Coefficient for Lead and Concrete, cm^2 / g

Energy of photon sources, MeV	Shielding materials	
	Lead	Concrete
10 [2]	0.02311	0.0497
20 [2]	0.02105	0.0621
30 [2]	0.02105	0.0702
40 [6]	0.0212	0.0765
50 [6]	0.0217	0.0811

Table 2. Specific Dose Coefficients for Photons of Different Energy Ranges, c Gy cm^2 / photon ×10^{-9}

Eγ	δ
0.1	0.0037
0.2	0.0086
0.5	0.238
1	0.45
2	0.756
3	1
4	1.22
5	1.43
6	1.62
8	2.01
10	2.33
15	3.26
20	4.26
30	6.19
40	8.13
50	10.6

The total absorbed dose rate was then calculated using Eq. (2):

$$\dot{D} = \int \varphi(E)\delta(E)dE. \tag{2}$$

FLUKA (Fasso et al., 2005) is a broadly useful tool for computations of particle transport and interactions with matter, covering a drawn-out scope of utilizations traversing from proton and electron accelerator shielding to target design. FLUKA can simulate of about 60 different particles with high exactness, including photons, electrons, neutrons, heavy ions, and antiparticles. The program can also transport polarized photons (e.g., synchrotron radiation) and optical photons. The lowest transport limit for all particles is 1 keV [7].

FLUKA Monte Carlo code gives a BEAM input file by which picking the particle kind, its energy, its direction and beginning position is conceivable. For more complicated circumstances, a dedicated "user routine" is liked. FLUKA input file comprises various data commands, each consisting of at least one line in the file [8], [9]. Input data for FLUKA were organised in a specific successive order according to code details. A simple cylinder geometry with the axis along the z-direction was described in the input file.

A concrete material was defined by a MATERIAL card in addition to as many COMPOUND words as required to describe concrete composition. The MATERIAL card used to define a compound composition carried the compound name, density, and material number (if input is explicitly number based) etc.

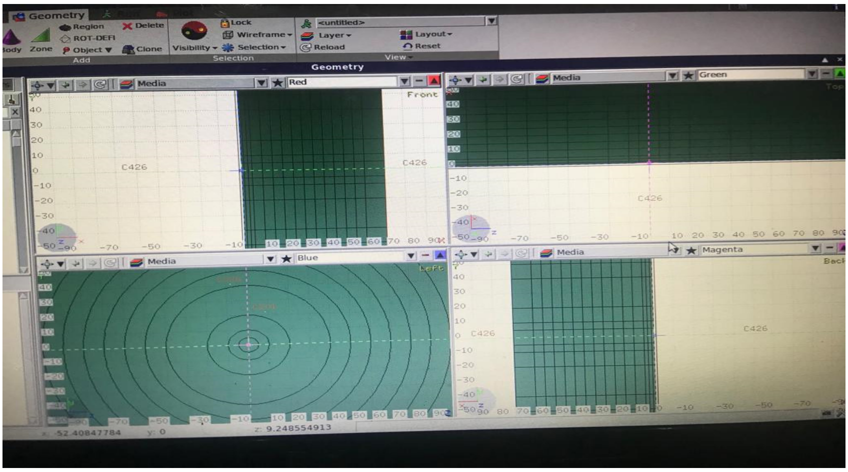

Fig. 2. Screenshot of Flair interface for top view of target geometry.

The transmission values were acquired utilizing USRBDX score card, after the code run for five cycles, with various sample thicknesses. USRBDX is the order used to characterise a detector for the boundary-crossing estimator. It calculates fluence, mono or bidirectional, differential in energy and angle on any boundary between two selected regions [2]. The uncertainty in transmission data values for all calculations was under 1%. Photon transmission results of simulations were taken from output files using Flair (see Fig. 2), which is FLUKA Advanced Interface, a data analysis interface compatible with FLUKA [10].

3. RESULTS AND DISCUSSION

Figure 3 shows the calculated spatial distributions of the absorbed dose in the air for concrete and lead shielding materials for two types of sources with the photon energy of 40 MeV. To compare both results, the results of the absorbed dose for the point isotropic source must firstly be multiplied by 4πR2, where R is the distance between the source and the detector. Then they can be compared with data for the flat unidirectional source. The comparison showed that the spatial distributions for all shielding materials at thicknesses up to 15 mfp were in a good agreement with an uncertainty of 5 %. The difference in large thicknesses of shielding, reaching up to 30 %, is due to uncertainty in the results for a unidirectional source. The dose rate resulting from the source's non-scattered radiation was calculated analytically, which made it possible to determine the dose factors of photon accumulation. The buildup factor depends on the angular distribution of the photons generated from the point isotropic source as shown in Table 3, Table 4, and Fig. 4. The exposure buildup factors of concrete for a point isotropic photon source with an energy of 10 MeV calculated by FLUKA are presented in Fig. 5. Also, Fig. 5 shows the exposure buildup factors of concrete for the flat unidirectional source with an energy of 10 MeV calculated by FLUKA. Furthermore, these results are also compared with results of other studies [1], [11]. The comparison shows an excellent agreement of about 5 %. Similarly, the exposure buildup factors of lead for a point isotropic photon source with an energy of 10 MeV calculated by FLUKA are presented in Fig. 6. Also, Fig. 6 shows the exposure buildup factors of concrete for the flat unidirectional source with an energy of 10 MeV calculated by FLUKA. In addition, these results are also compared with results of other studies [2], [3], [11]. The comparison shows an excellent agreement of about 5 %. These results indicate the reliability of the calculated results and the acceptability of the calculation method used.

Further investigations were done in this study. The buildup factors for lead obtained for monoenergetic photon sources in our study were compared with those buildup factors for lead presented in [12] for sources of bremsstrahlung photon radiation generated by electrons with different energies as seen in Fig. 7. The buildup factors for concrete obtained for monoenergetic photon sources in our study were compared with those buildup factors for concrete presented in [12] for sources of bremsstrahlung photon radiation generated by electrons with different energies. It was found that for all photon energies of the source, the buildup factors for monoenergetic sources were higher than the corresponding buildup factors for bremsstrahlung radiation sources as seen in Fig. 7.

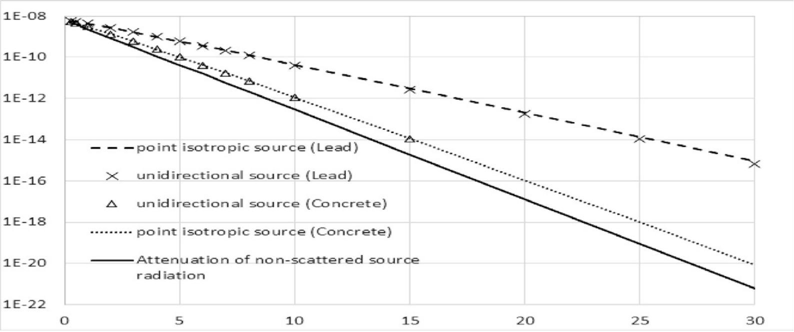

Fig. 3. Spatial distribution of the photon dose absorbed in lead, and concrete, from point isotropic and planar unidirectional photon sources with an energy of 30 MeV. Attenuation of non-scattered source radiation.

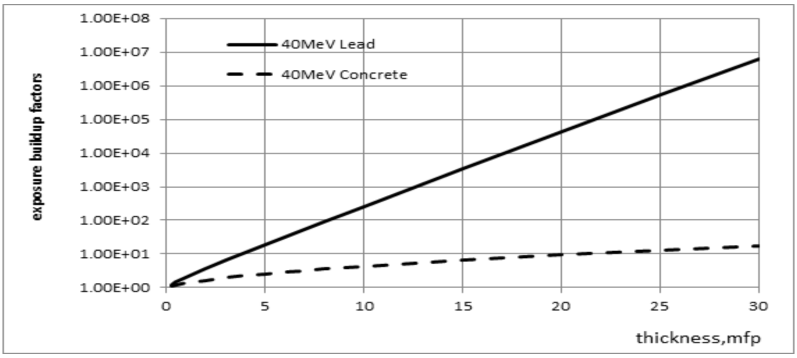

Fig. 4. Exposure buildup factors of photon in concrete and lead for a point isotropic photon source with energy of 40 MeV.

Table 3. Exposure Buildup Factors of Photon in Concrete and Lead Shielding for a Ppoint Isotropic Source with Photon Energy from 10 to 50 MeV

Material	Concrete					Lead				
E. MeV mfp	10	20	30	40	50	10	20	30	40	50
0.25	1.13	1.06	1.1	1.1	1.1	1.13	1.16	1.17	1.22	1.25
0.5	1.24	1.13	1.19	1.19	1.2	1.27	1.37	1.42	1.45	1.44
1	1.44	1.27	1.35	1.36	1.37	1.49	1.71	1.9	2.01	2.06
2	1.78	1.51	1.62	1.66	1.72	1.97	2.68	3.24	3.68	3.85
3	2.12	1.76	1.89	1.95	2.05	2.57	4.06	5.38	6.42	6.94
4	2.47	1.99	2.16	2.26	2.42	3.33	6.17	8.82	11.04	12.31
5	2.81	2.23	2.44	2.55	2.79	4.29	9.26	14.34	18.95	21.44
6	3.16	2.48	2.72	2.88	3.22	5.51	13.94	23.23	32.04	37.46
7	3.51	2.73	3.02	3.21	3.65	7.06	20.81	37.48	54.03	65.15
8	3.87	2.99	3.42	3.73	4.13	9.02	31.2	60.32	91.4	112.92
10	4.63	3.51	3.97	4.3	5.19	14.55	69.3	154	256	337
15	6.5	4.98	5.87	6.51	8.61	47.46	497	1603	3345	5049
20	8.56	6.63	8.12	9.32	13.68	150	3488	1.62E+4	4.23E+4	7.42E+4
25	10.74	8.34	11.38	12.77	20.54	461	2.38E+04	1.60E+05	5.28E+05	1.07E+06
30	12.79	9.11	14.81	17.58	27.46	1378	1.60E+05	1.55E+06	6.49E+06	1.51E+07

Table 4. Comparison of Exposure Buildup Factors of Photon in Concrete and Lead for a Point Isotropic Photon Source (FLUKA) with Energy of 10 MeV Obtained in Different Publications (P.S – point isotropic source, U.S – unidirectional source)

Material	Concrete				Lead				
Mfp	P.S	[1]	[11]	U.S	P.S	[2]	[3]	[8]	U.S
0.25	1.13			1.14	1.13				1.16
0.5	1.24	1.23	1.25	1.24	1.27	1.28	1.29	1.32	1.27
1	1.44	1.42	1.44	1.42	1.49	1.51	1.51	1.55	1.48
2	1.78	1.73	1.79	1.75	1.97	2.01	1.97	2	1.97
3	2.12	2.03	2.13	2.08	2.57	2.63	2.54	2.51	2.55
4	2.47	2.34	2.46	2.39	3.33	3.42	3.26	3.13	3.27
5	2.81	2.64	2.79	2.71	4.29	4.45	4.17	3.89	4.16
6	3.16	2.94	3.12	3.03	5.51	5.73	5.32	4.82	5.26
7	3.51	3.26	3.46	3.35	7.06	7.37	6.78	5.97	6.63
8	3.87	3.57	3.79	3.68	9.02	9.44	8.6	7.4	8.33
10	4.63	4.2	4.47	4.34	14.55	15.4	13.8	11.4	12.96
15	6.5	5.8	6.21	6.33	47.46	50.8	42.8	33.7	38.46
20	8.56	7.47	8		150	161	128	100	108.5
25	10.74	9.18	9.83		461	4.95E+02	3.69E+02	2.94E+02	3.89E+02
30	12.79	11	11.7		1378	1.47E+03	1.03E+03	8.52E+02	2.87E+03

As mentioned above, Tables 3 and 4 above show that the buildup factors in concrete and lead in the considered range of photon energies of the source depend on the angular distribution of the photons. In addition, the results presented in Tables 3 and 4 for point isotropic sources and for flat unidirectional sources are in a good agreement and the difference does not exceed 5 % for a given concrete thickness and does not exceed 10 % for lead thickness below 20 mfp. This leads to the conclusion that we can use any of both types of radiation sources when performing approximate shielding calculations. Depending on the photon energy of the source, the minimum values of the buildup factors for concrete are observed at energy of 20 MeV, and then they increase with the growth of the photon energy of the source. As the thickness of lead increases, the difference increases to 30 %, and the buildup factor for a point isotropic source is higher than the buildup factor for a flat unidirectional source.

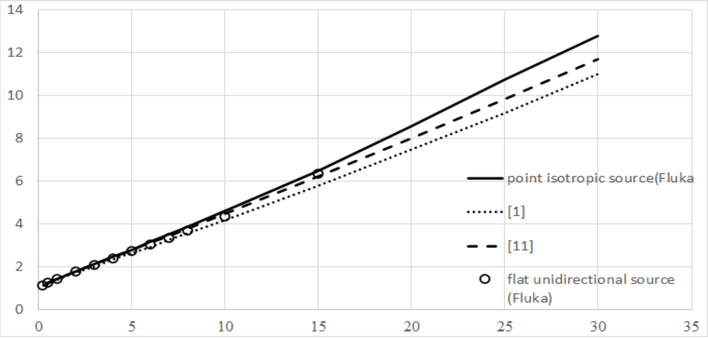

Fig. 5. Comparison of exposure buildup factors in concrete for a point isotropic photon source with energy of 10 MeV [1], [11].

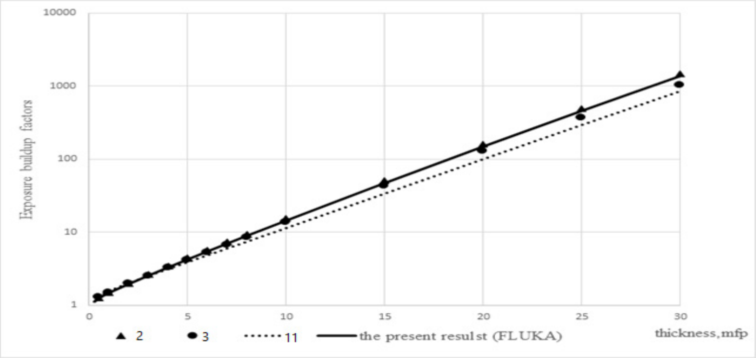

Fig. 6. Comparison of exposure buildup factors of photon in lead for a point isotropic photon source (FLUKA)with energy of 10 MeV [2], [3], [11].

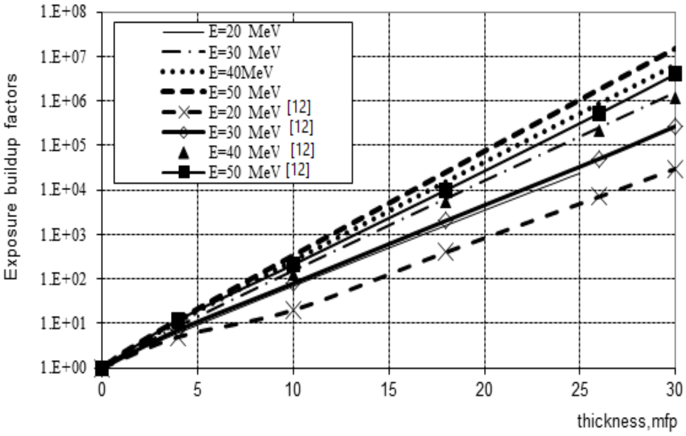

Fig. 7. Comparison of buildup factors of photon for lead obtained for monoenergetic photon sources in this paper and sources of bremsstrahlung [12].

4. AMENDMENT FOR THE BARRIER ENVIRONMENT FOR CONCRETE AND LEAD

Based on the results of calculations of the dose characteristics of photon fields in the materials under consideration in barrier geometry at shielding thickness of 5 and 10 mfp, amendment for barrier shielding was determined in the form of the ratio of buildup factor in barrier geometry to similar ones in an infinite medium. The calculated amendment was given for the materials under consideration in Tables 5 and 6; the amendment did not depend on the source photon energy and the protection thickness and was equal to 0.961±0.006 for concrete, and 0.982±0.004 for lead, respectively.

Table 5. Amendment for the Barrier Nature for a Medium of Concrete

mfp	5					10				
E, MэB	10	20	30	40	50	10	20	30	40	50
δ	0.950	0.964	0.964	0.962	0.970	0.950	0.954	0.962	0.959	0.968

Table 6. Amendment for the Barrier Nature for a Medium of Lead

mfp	5					10				
E, MэB	10	20	30	40	50	10	20	30	40	50
δ	0.979	0.979	0.980	0.980	0.980	0.982	0.978	0.982	0.978	0.976

5. CONCLUSIONS

Comparison of the calculated buildup factor with those available in the literature [2], [3], [6] for a photon source with an energy of 10 MeV, for concrete and lead showed their agreement within 5 %, which indicated the reliability of the calculated results and the acceptability of the calculation technique used. Moreover, some overestimation of the buildup factor obtained in this work more coincides with reality, since our calculations took into account all the processes of interaction of photons with matter, but the result in the literature did not take into account the coherent scattering of photons, which led to noticeable errors in calculation of the buildup factor obtained in these works.

Based on the results of calculations of the dose characteristics of photon fields in the materials under consideration in the barrier geometry at shielding thickness above 3 *mfp*, amendment for the barrier shielding was determined in the form of the ratio of buildup factors in the barrier geometry to similar ones in an infinite medium. In the considered range of material thickness, the amendment did not depend on the source photon energy and the shielding thickness and was equal to 0.960±0.006 for concrete, and 0.982±0.004 for lead, respectively.

REFERENCES

1. Sakharov, V. K., & Borisenko, A. V. (2014). Photon Dose Accumulation Factor in Concrete, Iron, and Lead for 10–50 Mev Microenergetic Sources. *Atomic Energy, 114*, 225–228. doi:10.1007/s10512-014-9845-9
2. American National Standard. (1991). *Gamma-Ray Attenuation Coefficients and Buildup Factors for Engineering Materials*. ANSI/ANS-6.4.3-1991.
3. Durani, L. (2009). *Update to ANSI/ANS-6.4.3-1991 for Low-Z and Compound Materials and Review of Particle Transport Theory.* PhD Thesis. Available at http://dx.doi.org/10.34917/1363554
4. Mashkovich, V.P., & Kudryavtseva A.V. (1999*). Protection from Ionizing Radiation*. Reference book. Moscow: Energoatomizdat.
5. Fasso, A., Ferrari, A., & Sala, P. R. (2001). Electron – photon transport in FLUKA: Status. In *Proceedings of the Advanced Monte Carlo for Radiation Physics, Particle Transport Simulation, and Applications* (pp. 159–164), Lisbon, 2000. Berlin; Heidelberg: Springer.
6. Storm, E., & Israel', K.H. (1973). *Cross Sections for the Interaction of Gamma Radiation*. Spravochnik. Per. s angl. Pod red. Klimanova V. A. Chistova Ye.D. M. Atomizdat. (in Russian).
7. Patil, B. J., Chavan, S. T., Pethe, S. N., Krishnan, R., Bhoraskar, V. N., & Dhole, S. D. (2010). Simulation of e–γ–n Targets by FLUKA and Measurement of Neutron Flux at Various Angles for Accelerator Based Neutron Source. *Annals of Nuclear Energy, 37* (10), 1369–1377. http://dx.doi.org/10.1016/j.anucene.2010.05.009
8. Ferrari, A., Sala, P. R., Fasso, A., & Johannes, R. (2005). *FLUKA: A Multi-Particle Transport Code* (Program version 2005). Geneva: CERN. Doi: 10.5170/cern-2005-010.
9. Mark, S., Khomchenko, S., Shifrin, M., Haviv, Y., & Schwartz, J. R. (2007). TVF-NMCRC—A Powerful Program for Writing and Executing Simulation Inputs for the Fluka Monte Carlo Code System. *Nuclear Instruments and Methods in Physics Research. Section A, Accelerators, Spectrometers, Detectors and Associated Equipment, 572* (2), 929–934. https://doi.org/10.1016/j.nima.2006.12.007
10. Vlachoudis, V. (2009). FLAIR: A powerful but user-friendly graphical interface for FLUKA. In *International Conference on Mathematics, Computational Methods & Reactor Physics 2009*, (pp. 790–800). 3–7 May 2009, Saragota Springs, New York.
11. Ashimizu, A., Onda, T., & Sakamoto, Y. (2004). Calculation of Gamma-Ray Buildup Factors up to Depths of 100 mfp by the Method of Invariant Embedding, (III). J. *Nucl. Sci. and Technology, 41* (4), 413–424.
12. Bespalov, V.I. (2011). *Lectures on Radiation Protection*. Study guide (3rd ed.) Tomsk: Publishing House of Tomsk Polytechnic University. (in Russian).

LATVIAN JOURNAL OF PHYSICS
AND TECHNICAL SCIENCES
2024, N 1

DOI: 10.2478/lpts-2024-0003

SODIUM CITRATE AND POLYVINYLPYRROLIDONE CAPTURED SILVER NANOPARTICLES TRANSFER TO ORGANIC SOLVENTS

J. Mikelsone, A. Vembris*

Institute of Solid State Physics, University of Latvia
8 Kengaraga Str, Riga, LV1063, LATVIA
*e-mail: aivars.vembris@cfi.lu.lv

Silver nanoparticles (NPs) have gathered extensive attention due to their properties – chemical stability, good conductivity, catalytic activity, and antimicrobial activity. This makes NPs suitable for potential applications in the development of new technologies in the field of photonics, electronics, medicine, biochemical sensing, and imaging. Nanoprisms have local surface plasmon resonance starting from visible to near infra-red spectrum, broadening the possibilities of their applications. Ag NPs typically are synthesized in aqueous solution but the handling of NPs often requires their dispersion into nonpolar solvents and their mixing with organic compounds. Thus, nanoparticle transfer to organic media is essential for application in the field of emission enhancement due to NPs – organic semiconductor interaction. A shell changing method for NP tranfer was successfully used with a high transfer rate, but rather low stability. The previously proposed sonochemical method for NP transfer from aqueous to organic polymeric media is extended to different organic solvents. The ultrasonic method is suitable to obtain stable NPs in both organic solvent and organic solvent/organic compound solutions, and it can be stored at ambient conditions for at least several months. Transfer efficiency is suficient and NPs remain stable in an organic solvent like chlorobenzene, anisole, dichloromethane. The method has potential in NPs containing thin film preparation because sonication prevents the agglomeration of clusters.

Keywords: *Changes of shell, chemical synthesis, silver nanoprism, transfer to organic solvents.*

1. INTRODUCTION

Metal nanoparticles (NPs) have been a very active research object due to the local surface plasmon resonance (LSPR) effect that can be used in various applications, such as sensors, photovoltaic and Raman spectroscopy [1]–[3]. Surface plasmon enhanced fluorescence (PEF) is an important effect to improve the emission properties of the semiconductor. It offers higher emission efficiency and decreased lifetime via the local electric field enhancement effect of the metal nanoparticles induced by its LSPR [4]–[6]. Initially, the emission enhancement was achieved in inorganic semiconductors, but recently more systems consisting of organic semiconductors were tested. It is driven by the growing potential of organic materials in the light-emitting diodes, photovoltaics and solid-state lasers [7], [8].

Nevertheless, metallic nanoparticle – organic compound systems face several issues. Preparation of the nanoparticles with controlled size, shape and distribution, which is essential for emission enhancement, and transferring of nanoparticles in organic solvent could be considered as the most important. Synthesis of specific size and shape of nanoparticles is important because it determines the spectrum of LSPR, which in turn should match the emission spectrum of an organic dye to get the highest enhancement [9]. Metallic nanoparticles most efficiently can be synthesized in an aqueous solution, but organic materials usually cannot be dissolved in water; therefore, metal nanoparticles should be transferred to the organic solvent, like chloroform or toluene. For this reason, the nanoparticle's shell should be changed to one which can disperse the nanoparticle in the organic solvents.

In the literature, there are several methods to disperse the nanoparticles in organic solvents – NP transfer from aqueous solution by shell changing, centrifugation, solvent evaporation and NP powder redispersion in organics [10]–[13], silver nanoparticles can be synthesised directly in an organic solvent like toluene [14], [15]. Despite so many methods, there are still several challenges associated with NP transfer to organic media, like transfer efficiency, repeatability and stability. NP stability in organics is temporal and NP agglomerates in a short period of time – from a few hours to some days.

In this study, a well-described method of NP synthesis in an aqueous solution was used [11], [16]. Nevertheless, most of the syntheses resulted in another size of NPs than expected from literature. The difference is related to the procedure of adding the reducing agent, so the amount, time interval and frequency of the reducing agent were studied in more detail. Synthesised NPs were transferred to organic solutions by two of the most promising transfer methods – shell changing and transfer during sonification. Shell changing transfer method is described in many papers [12] and it gives the best repeatability of the transfer process, but a chemical synthesis of a new shell is required, which complicates the process. Phase transfer during sonification is simple to use, but repeatability is lower, and some degradation of nanoparticles may occur. Ultrasonic method has been used only for one solvent/polymer system and chemical methods have been mostly applied to nanospheres [13]. The possible nanoprism transfer to different organic solvents and organic solvent/organic compound systems with and without the change of shell by using both methods were extended.

2. MATERIALS AND METHODS

All the reagents and solvents were used as received without any further purification: $AgNO_3$ (≥99.8 %, Supelco), Polyvinylpyrrolidone (PVP, M_w ~29000, Sigma Aldrich), sodium citrate (USP), hydrogen peroxide solution (30wt%, Sigma-Aldrich), sodium borohydride (NaBH4, ≥98 %, Sigma-Aldrich), deionized water, ethanol (96 %), dichloromethane (DCM, ≥99.8 %, Sigma-Aldrich), chlorobenzene (≥99.8 %, anhydrous, Sigma-Aldrich), 1,2 Dichlorobenzene (99 % Alfa Aesar), anisole (99.7 %, Sigma-Aldrich), toluene (99.8 %, anhydrous, Sigma-Aldrich), Tris-(8-hydroxyquinoline)aluminum (Alq3, 99.995 %, Sigma-Aldrich), hexadecyltrimethylammonium bromide (CTAB, 99+ %, ACROS Organics™), 2-Aminoethanethiol (99,9 %, Flourochem), oleic acid (99 %, Alfa Aesar), Hydroxylamine hydrochloride (99+ %, ACROS Organics™), methanol (≥99.9 %).

Synthesis of Silver Nanoparticles in aqueous solution: Silver nanoprisms were synthesized by borohydride reduction of $AgNO_3$ [11], [16]. Sodium citrate (9.2 mM 5 ml), PVP (0.2 mM 5 ml), H_2O_2 (30 wt%, 60 ml) while stirred with magnetic bar at ambient conditions were added to aqueous solution of AgNO3 (0.19 mM 18 ml). Afterwards, $NaBH_4$ (100mM 70–250 ml) was added to obtain NP solutions with different absorption peak and nanoprism size (Fig. 1). A synthesis outcome dependence on added reductant procedure will be discussed further.

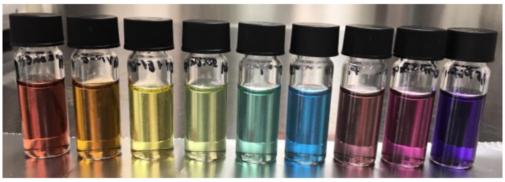

Fig. 1. Synthesized Ag NPs aqueous solutions with different nanoprism size.

The absorbance spectra of NPs solutions were measured with spectrophotometer Cary 7000, shape and size of NPs were studied with TEM Fei Technai, Z-potential values and hydrodynamic diameter of NPs were measured by Anton Paar Litesizer™ 500.

3. RESULTS AND DISCUSSION

According to the literature, the amount of $NaBH_4$, added to the solution during the synthesis of NPs, defines the size of NP and LSPR wavelength [11], because $NaBH_4$ affects NP shell formation and bounding ability of sodium citrate to Ag NPs [16]. A greater amount of borohydrides promotes citrate bounding to Ag^0; thus, NPs are forming faster and the prism size is bigger. If a reduction agent is added in smaller parts, it is possible to obtain smaller nanoprisms.

Nevertheless, during the synthesis it was noticed that the different sizes of NPs could be obtained in a solution by adding the same amount of $NaBH_4$. The difference was in the adding frequency and the period of time between additions of $NaBH_4$. To the best of our knowledge in the literature there is not mentioned the adding procedure impact on size of the NPs. The same amount can be added at once or in several parts. Greater NPs form if $NaBH_4$ solution was added at once. If a small part of $NaBH_4$ is added, silver spherical nanoseeds form in solution, further adding of $NaBH_4$ allows obtaining greater NPs. Thus, the amount and adding frequency of $NaBH_4$ is a crucial factor in the nanoprisms synthesis.

If more than 120 ml $NaBH_4$ solution is added simultaneously, blue NPs solution is obtained, indicating the formation of the greater nanoprisms. Red nanoprism aqueous solution can be obtained by adding 50 ml $NaBH_4$ solution to well stirred $AgNO_3$, sodium citrate, PVP solution immediately after H_2O_2 was added. Then 20 ml more $NaBH_4$ solution should be added after 2 min. Another factor affecting synthesis is $NaBH_4$ reaction with water, which can be observed as gas evolution from solution [17]:

$$NaBH_4 + 2\ H_2O \rightarrow NaBO_2 + 4\ H_2.$$

Sodium borohydride solution should be prepared shortly before use and the temperature of the solution should be decreased to inhibit the reaction.

Moreover, external influence also should be considered. Ambient light impacted not only the process of synthesis but also the stability of the NPs. Nanoprism formation delay after reductant addition increased at more intensive ambient light. The period of time between nanoprism formation indicated by solution color changes after reductant addition at the dim light is 2–3 minutes, but at bright light – 30 min, which is mentioned in [11], [12].

Two NPs aqueous solutions were characterised and used for NP transfer to organic media. Optical absorption of selected solvents is shown in Fig. 2. Chosen solvents had red (further referred to as "Red NPs" in the text) and blue (further referred to as "Blue NPs" in the text) colour.

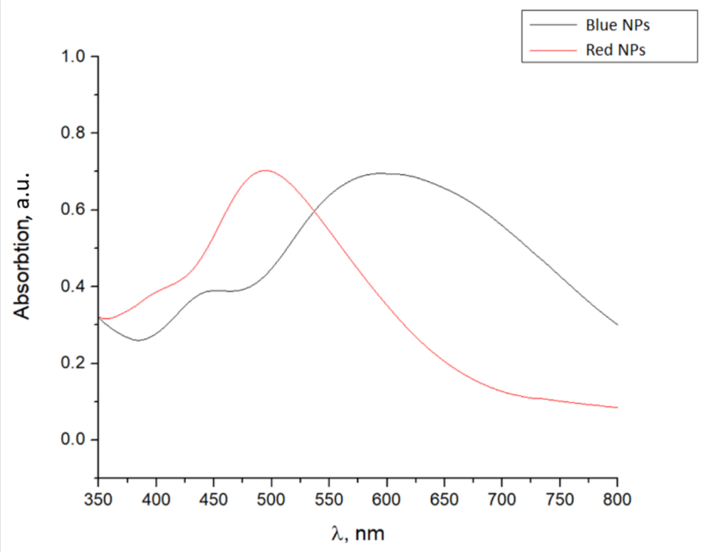

Fig. 2. Absorbance spectra of Blue NPs and Red NP solutions.

A hydrodynamic diameter (HD) and Z-potential (ZP) of the investigated NPs are presented in Table 1. The value of ZP for Red NPs solution measured shortly after synthesis is ξ = -10.89 mV indicating instability of the NPs [18]. The stability of Red NPs increases and the ZP value of the solution became ξ -16.51 mV after two weeks stored in the dark. An HD of the NPs increases and FWHM (full width at half maximum) broadens about 2.4 times. The HD of Red NP sample has values in the range from 27.49 to 76.90 nm and the same solutions measured after 14 days had HD values in the range from 26.19 to 146.23 nm. Thus an HD of ~27nm is related to single NP in the solution, but greater HD indicates small cluster formation in the solution. There are no changes in the second peak; thus, there is no NP decomposition. At the same time, a ZP value became more negative, so the stability increased. It could be explained by the formation of more regular NP cluster forms. An HD does not change for freshly synthesized and ultrasound treated NPs stored for 2 weeks, but ultrasound treatment improves ZP values two times. Ultrasound separates NPs from each other and repulsive surface forces become predominant. TEM images are shown in Figs. 3 and 4. Red NPs shortly after synthesis are glued together, what is the reason of the low ZP value. After Red NPs solution sonication for 2h, NPs became very well dispersed and only individual NPs could be seen in the TEM field of view. Ultrasonically separated NPs one from the other and repulsive surface forces overcame attraction surface forces, which held NPs together in agglomerates/clusters. After an additional 1 h in ultrasonic bath degradation of NPs starts and a great number of smaller NPs can be seen, while HD values in the first and second peak do not change.

ZP measurements show good stability of freshly synthesized Blue NPs, but HD values show a reduction of NPs size after 2 weeks. Sonification leaves no impact on Blue NPs ZP, thus, on stability. The ultrasonic treatment leaves no impact on HD of Blue NPs stored for 2 weeks. For all solutions, there are decrement in HD value. Blue NPs shortly after synthesis are well separated and no agglomerates are seen. After sonification of 2 h only individual NPs can be seen on the TEM field of view, similar to the Red NPs. No additional number of smaller NPs was observed after 3 h of sonification; thus, Blue NPs do not require stabilization after synthesis. Still, we suggest 0.5–1 h sonification for Blue NPs, because in the few synthesized aqueous NP solutions slight agglomeration of Blue NPs was observed. There are no spectral changes for most of blue nanoparticles synthesis or they are very seldom, in contrast – Red NP aqueous solution tends to change absorption peak towards the red spectral region and some red solutions change their colour to blue.

Table 1. Hydrodynamic Diameter and Z-Potential Values of Red NP and Blue NP Solutions

Sample	HD_{1peak}, nm	FWHM±ΔFWHM, nm			HD_{2peak}, nm	FWHM±ΔFWHM, nm			Z-potential, mV±DmV		
Red NPs	52.19	49.4	±	1.5	4.39	2.57	±	0.09	10.89	±	0.56
Red NPs *	86.21	120.0	±	7.8	5.86	4.91	±	0.31	16.51	±	0.57
Red NPs +2hus*	52.68	48.0	±	1.2	5.00	3.43	±	0.13	18.44	±	0.85
Red NPs +2+1hus*	54.58	53.2	±	2.6	5.12	3.69	±	0.12	20.76	±	1.03
Red NPs in_chlorbenzene	8.68	3.1	±	0.3	0.50						
Red NPs in DCM	7.44	2.8	±	0.4	-						
Blue NPs	52.96	54.7	±	3.1	2.55	3.18	±	0.27	21.82	±	1.09
Blue NPs *	42.33	38.3	±	1.1	2.62	1.89	±	0.08	20.53	±	0.99
Blue NPs +2hus*	41.27	39.8	±	2.5	2.33	2.07	±	0.10	23.70	±	1.14
Blue NPs +2+1hus*	38.34	32.3	±	1.6	2.33	1.76	±	0.08	20.65	±	1.02
Blue NPs in DCM	8.68	2.8	±	0.3	-						
Blue NPs in anisole	97.66	53.9	±	3.60	-						

* - measurements performed 14 days after synthesis

TEM data show that NP size in Red and Blue NP solutions fits lognormal distribution (Fig. 5). The mean value of Red NPs is smaller according to the literature data [19], [20]. However, size distribution is affected by a high amount of nanospheres, since nanospheres and nanoprisms have different absorption peaks. A standard deviation of size distribution is rather high indicating a variety of NP size and shape in synthesized solution. Comparison of TEM and HD data shows that thickness of NP shell is roughly 10 nm. Thus such NPs can be used for energy transfer from NPs to surrounding molecules, like luminescent molecules [21], [22] for SRP enhanced luminescence.

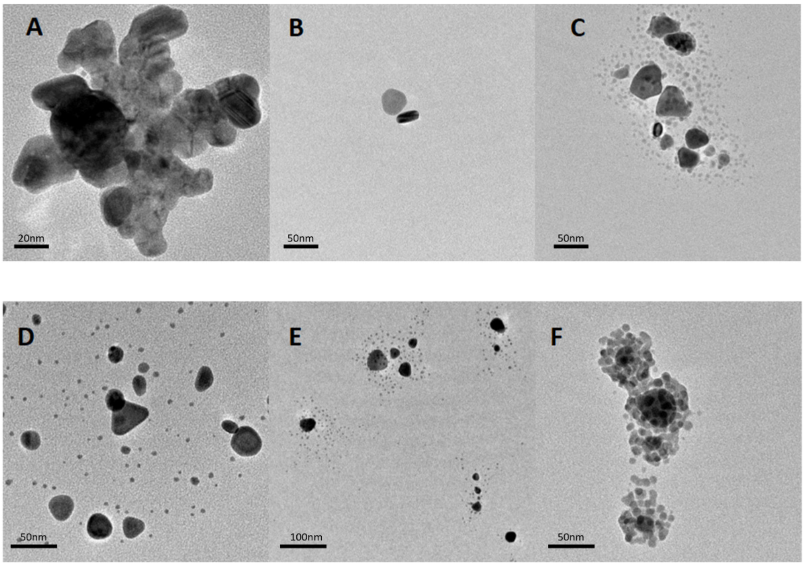

Fig. 3. TEM images of Red NPs solution. A – solution shortly after synthesis; B – after 2 h sonification; C – after 2 h+1 h sonification; D – NPs in anisole; E – NPs in chlorobenzene; F – NPs in DCM.

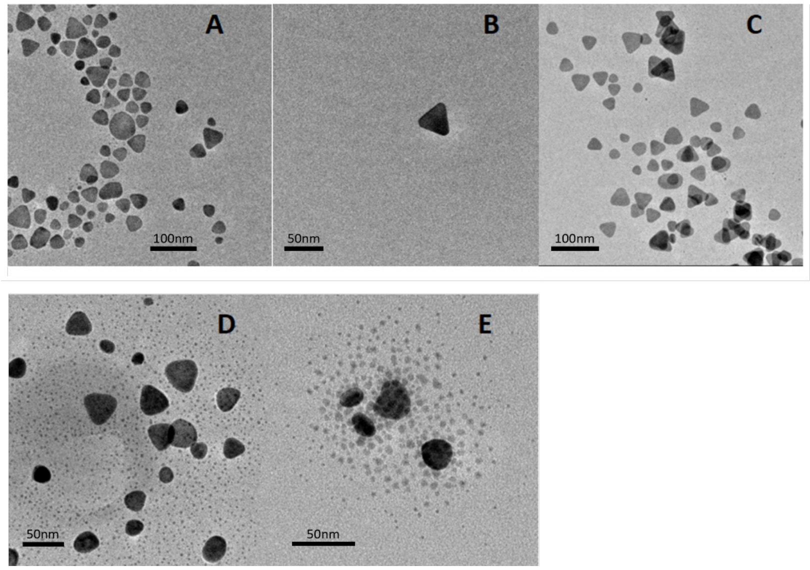

Fig. 4. TEM images of Blue NPs solution. A – solution shortly after synthesis; B – after 2 h sonification; C – after 2 h+1 h sonification; D – NPs in chlorobenzene; E – NPs in DCM.

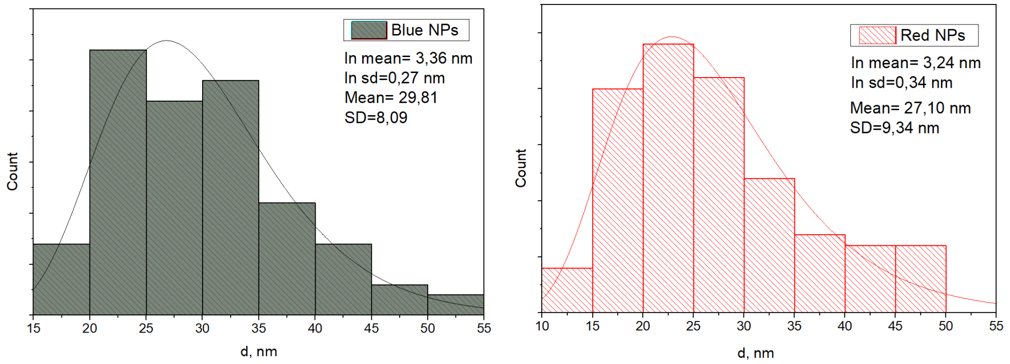

Fig. 5. NPs size distribution obtained from TEM data; on the left – Blue NPs, on the right – Red NPs.

Silver nanoparticles transfer from aqueous to organic solvents:

In literature, sonochemical method was used to transfer spherical NPs to polymethylmethacrylate (PMMA) dissolved in organic solvent [13]. No other materials were tested, thereby applications of the method were limited. Nevertheless, the transfer efficiency was high. More organic compounds were tested to approve the method. We transferred prismatic NPs to PMMA, polystyrene, polysolfone (Fig. 6).

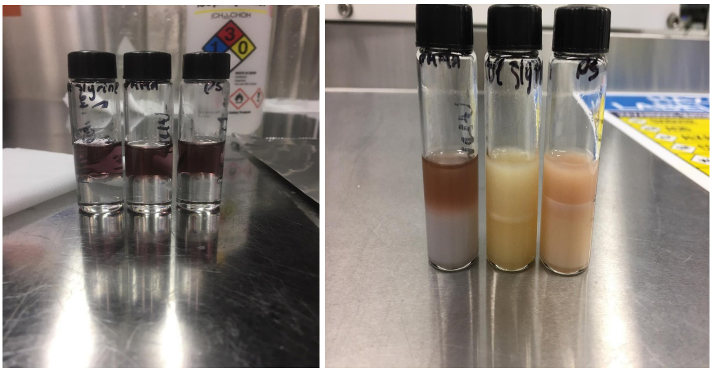

Fig. 6. On the left – polymer in DCM and NP aqueous solution; on the right – NP transfer to polymer+DCM solution. Upper layer – aqueous solution, lower layer – NPs –polymer+DCM solution. From left to right – PMMA, polystyrene, polysolfone.

Moreover, NP transfer to organic solvent without organic compound additives would be an even more general approach. In that case, any organic compounds could be dissolved in the metal NP containing solvent afterwards.

The NP transfer to organic solvent was performed. Ethanol of 10ml, which acts as a bounding element, was added to 3ml of synthesized NP aqueous solution. The solution was stirred for ~2–5 minutes, then 3 ml of DCM or another organic solvent (chlorobenzene, anisole) was added. The obtained solution was placed in an ultrasonic bath (37 kHz) for 2–3 h. Aqueous solvent partially or completely discolored indicating the absence of NPs (Fig. 6). After NP transfer process, white precipitate formed that could be complex citrate compounds. Silver is not a component of precipitate, since the same precipitate forms if pure sodium citrate solution in water is used instead of

NPs solution. The precipitate decomposes if solution is stored for 1 week in the dark. A white precipitate forms a segregated layer between the organic and aqueous phase and can have (not always) colour of NP aqueous solution. Figure 6 shows solutions before and after blue NP transfer to organic media. Similar results can be obtained with Red NPs. Precipitate settles between both phases after a few hours. Despite the presented organic solution with visible absorption in visible range after the transfer, the organic phase is colourless when it is separated from aqueous solution and poured to other flask (Fig. 8). Solution with absorption in a visible range is located around the organic phase. The media could be partially transferred NPs, which can be dissolved neither in an aqueous nor in an organic phase. Partially transferred NP is just a suggestion, it is not based on experimental or theoretical results.

NPs in the organic phase are colourless due to the change of the dielectric constant of the solvent [23]. NPs in aqueous solution experience changes before and during ultrasonic treatment: ethanol can change the spectrum before sonication since it acts as a reducing agent in the nanoparticles synthesis [24], [25]. NP solution can change colour during sonification, which indicates the size change or breakup of the nanoprisms. This process can be promoted by sodium citrate reducing properties in an aqueous solution under ultrasonic treatment [26], [27].

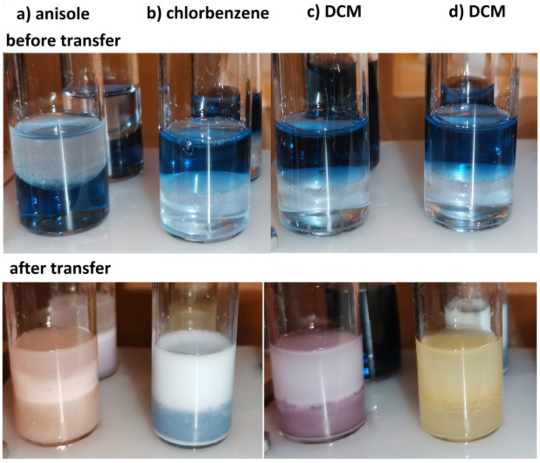

Fig. 7. NPs transfer to organic solvents. The upper picture is taken before sonication, bottom – after.

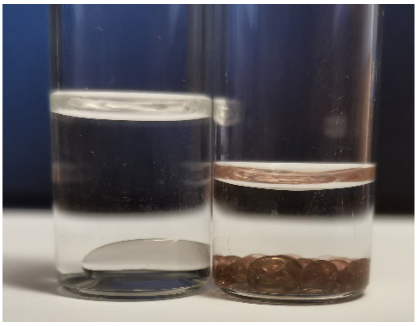

Fig. 8. On the left – NPs transfered to DCM before extraction; NPs transfered to DCM after extraction.

TEM investigation shows a significant number of NPs in organic phase in all used solvents – anisole, DCM and chlorobenzene (Fig. 3 D, E, F and Fig. 4. D and E). In chlorine containing organic solvents nanoparticles fall to pieces. HD measurements do not show a peak at 30–50 nm, only at ~10 nm indicating strong NP decomposition. In anisole, there is a significant amount of small (~10nm) nanoparticles, but the number of nanoprisms overcomes them and no considerable decomposition is observed. HD measurements in anisole were affected by white precipitate and no data could be obtained for red NPs.The ultrasonic method provides stable NPs in organic media but a low transfer rate. Nevertheless, NPs in organic media can be mixed with any organic soluble luminophore, polymer or other material for futher applications.

According to the literature, changing the shell of NPs allows achieving a higher transfer rate [28]. For this reason, synthesized NPs were transferred to organic media (DCM) by changing the shell from sodium citrate + PVP to thiol-termination ligand [16]. Thiol has a great affinity to metallic particles and can easily replace PVP and sodium citrate shells. The synthesis of the ligand is described elsewhere [16]. 1 ml of thiol-termination ligand solution was added to 2 ml of aqueous NP solution. The solution was vigorously stirred, then it was left at room temperature for 1 h. Afterwards, 2 ml of DCM were added, then the solution was stirred until NP transfer to organic media was obvious. After the exchange of shell NPs in organic media solution colour corresponds to the initial aqueous solution. Organic solution became yellow after 12 to 24 hours. TEM investigation showed that prisms sticked together (see Fig. 9), which made changes in SPR wavelength. NPs stability in organic media did not exceed one week, resulting in NP agglomeration and precipitation. The shell that allows dispersing NPs in organic media is oily; thus, the thickness of the shell is large. Litesizer 500 measurements show a very high value of HD exceeding 1 mm, while TEM data do not show considerable changes in NP size. Such NPs can be used for NP introduction into organic media. Despite low stabillity, NPs with changed shell can be successfully used shortly after phase change for nanoparticles containing organic thin film preparation with application in different field, like light emission enhancement.

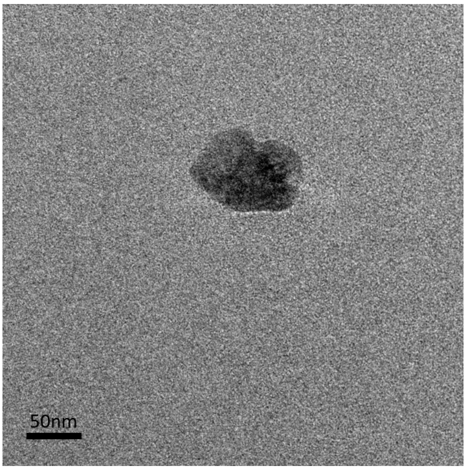

Fig. 9. Ag nanoparticle with changed shell.

4. CONCLUSION

In this study, silver prismatic nanoparticles with PVP + sodium citrate shell were synthesized. The size of NPs can be changed by varying added amount and frequency of $NaBH_4$. Ultrasound treatment separates NPs in an aqueous solution and increases their stability. Obtained nanoparticles can be transferred to organic media, like DCM, chlorobenzene using the sonochemical method or shell replacing. The second method is more effective for NP transfer to organic media, but it is more difficult. The introduction of NPs in organic media should be done shortly after NP transfer to organic solvent due to the low stability of the NPs. Transfer of NPs to organic media by the ultrasonic method is easier and NPs remain stable for a month at ambient conditions. NPs can be dispersed in a solution volume using an ultrasonic bath. It could be an advantage for organic material containing NP thin film preparation, where there are problems with NP clumping and inhomogeneous dispersion within a volume of a thin film.

ACKNOWLEDGEMENTS

The research has been funded by the Latvian Council of Science, project "Surface Plasmon Resonance Enhanced Light Amplification and Modulation in Organic Thin Films", No. lzp-2019/1-0441.

The Institute of Solid State Physics of the University of Latvia as the Center of Excellence has received funding from the European Union's Horizon 2020 Framework Programme H2020- WIDESPREAD-01-2016-2017-TeamingPhase2 under grant agreement No. 739508, project CAMART^2.

REFERENCES

1. Khan, I., Saeed, K., & Khan, I. (2019). Nanoparticles: Properties, Applications and Toxicities. *Arabian Journal of Chemistry, 12*, 908–931. DOI:10.1016/j.arabjc.2017.05.011
2. Duan, L, & Uddin, A. (2020). Progress in Stability of Organic Solar Cells. *Adv. Sci. 2020, 7*, 1903259. DOI:10.1002/advs.201903259
3. Lu, J., Cai, Z., Zou, Y., Wu, D., Wang, A., Chang, J., … & Liu, G. (2019). Silver Nanoparticle-Based Surface-Enhanced Raman Spectroscopy for the Rapid and Selective Detection of Trace Tropane Alkaloids in Food. *ACS Appl. Nano Mater., 2* (10), 6592–6601. DOI:10.1021/acsanm.9b01493
4. Du, Y., Alifu, N., Wu, Z., Chen, R., Wang, X., Ji, G., … & Song, D. (2020). Encapsulation-Dependent Enhanced Emission of Near-Infrared Nanoparticles Using in vivo Three-Photon Fluorescence Imaging. *Front. Bioeng. Biotechnol., 8*, 1029. DOI:10.3389/fbioe.2020.01029
5. Li, J.-F., Li, C.-Y., & Aroca, R.F. (2017). Plasmon-Enhanced Fluorescence Spectroscopy. *Chem. Soc. Rev.*, *46*, 3962–3979. DOI:10.1039/C7CS00169J
6. Li, Q., Kamra, T., & Ye, L. (2016). Nanoparticle-enhanced fluorescence emission for Non-Separation Assays of Carbohydrates Using a Boronic Acid–Alizarin Complex. *Chem. Commun., 52,* 3701–3704. DOI:10.1039/C5CC10516A

7. Zou, Y., Gong, S., Xie, G., & Yang, C. (2018). Design Strategy for Solution-Processable Thermally Activated Delayed Fluorescence Emitters and Their Applications in Organic Light-Emitting Diodes. *Advanced Optical Materials, 6,* 1800568. DOI:10.1002/adom.201800568
8. Jiang, Y., Liu, Y.-Y., Liu, X., Lin, H., Gao, K., Lai, W.-Y., & Huang, W. (2020). Organic Solid-State Lasers: A Materials View and Future Development. *Chemical Society Reviews, 49,* 5885–5944. DOI:10.1039/D0CS00037J
9. Movsesyan, A., Lamri, G., Kostcheev, S., Horneber, A., Bräuer, A., Meixner, A.J., … & Adam, P.M. (2020). Enhanced Two-Photon Photoluminescence Assisted by Multi-Resonant Characteristics of a Gold Nanocylinder. *Nanophotonics, 9*, 4009–4019. DOI:10.1515/nanoph-2020-0213
10. Maity, J., Chowdhury, A. H., Islam, Sk M., Balaet, T. (2020). A Facile Route to Transfer Cu Nanoparticles to Organic Medium for Better Stabilization and Improved Photocatalytic Activity Towards N-Formylation Reaction. *Nanotechnology, 31,* 395605. DOI:10.1088/1361-6528/ab9574
11. Kulkarni, A.P., Munechika, K., Noone, K.M., Smith, J.M., & Ginger, D. (2009). Phase Transfer of Large Anisotropic Plasmon Resonant Silver Nanoparticles from Aqueous to Organic Solution. *Langmuir*, *25*, 7932–7939. DOI:10.1021/la900600z
12. Zhang, Q., Li, N., Goebl, J., Lu, Z., & Yin, Y. (2011). A Systematic Study of the Synthesis of Silver Nanoplates: Is Citrate a "Magic" Reagent?. *J. Am. Chem. Soc., 133,* 18931–18939. DOI:10.1021/ja2080345
13. Goyal, A., Rozra, J., Saini, I., Sharma, P.K., & Sharma, A. (2012). Refractive Index Tailoring of Poly(methylmethacrylate) Thin Films by Embedding Silver Nanoparticles. *Advanced Materials Research, 585,* 134–138. DOI:10.4028/www.scientific.net/AMR.585.134
14. Lu, L., & An, X. (2015). Silver nanoparticles synthesis using H2 as reducing agent in toluene–supercritical CO2 microemulsion, *The Journal of Supercritical Fluids, 99*, 29–37. DOI:10.1016/j.supflu.2014.12.024
15. Wang, X., Zhao, Z., Ou, D., Tu, B., Cui, D., Wei, X., & Cheng, M. (2016). Size-Controlled Synthesis of Silver Nanoparticles from Silver Mirror Reaction in Toluene. *Micro & Nano Letters, 11*, 454–456. DOI:10.1049/mnl.2016.0099
16. López-Millán, A., Zavala-Rivera, P., Esquivel, R., Carrillo, R., Alvarez-Ramos, E., Moreno-Corral, R., Lucero-Acuña, A. (2017). Aqueous-Organic Phase Transfer of Gold and Silver Nanoparticles Using Thiol-Modified Oleic Acid. Appl. Sci., 7, 273. DOI:10.3390/app7030273
17. Demirci, U. B., Akdim, O., Andrieux, J., Hannauer, J., Chamoun, R., & Miele, P. (2010). Sodium Borohydride Hydrolysis as Hydrogen Generator: Issues, State of the Art and Applicability Upstream from a Fuel Cell. *Fuel Cells, 10,* 335–350. DOI:10.1002/fuce.200800171
18. Sun, D., Kang, S., Liu, C., Lu, Q., Cui, L., & Hu, B. (2016). A Brief Review on Electrode Materials for Supercapacitor. *Int. J. Electrochem. Sci., 11*, 8520–8529. DOI:10.20964/2016.10.30
19. Pastoriza-Santos, I., & Liz-Marza´n, L.M. (2008). Colloidal Silver Nanoplates. State of the Art and Future Challenges. *J. Mater. Chem., 18,* 1724–1737, DOI:10.1039/b716538b
20. Saade, J., & de Araújo, C.B. (2014). Synthesis of Silver Nanoprisms: A Photochemical Approach Using Light Emission Diodes. *Materials Chemistry and Physics, 148*, 1184–1193, DOI:10.1016/j.matchemphys.2014.09.045
21. Vembris, A., Zarins, E., Jubels, J., Kokars, V., Muzikante, I., Miasojedovas, A., & Jursenas, S. (2012). Tailoring the Optical Limiting Response of Methyl Orange via Protonation. *Opt. Mater., 34*, 1501., DOI:10.1016/j.optmat.2012.02.051
22. Vembris, A., Zarins, E., & Kokars, V. (2015). Solid State Solvation Effect and Reduced Amplified Spontaneous Emission Threshold Value of Glass Forming DCM Derivative in PMMA Films. *Journal of Luminescence, 158,* 441–446, DOI:10.1016/j.jlumin.2014.10.050

23. Wan Mohd Ebtisyam Mustaqim Mohd Daniyal, Yap Wing Fen, Jaafar Abdullah, Amir Reza Sadrolhosseini, Mohd Adzir Mahdi. (2021). Design and Optimization of Surface Plasmon Resonance Spectroscopy for Optical Constant Characterization and Potential Sensing Application: Theoretical and Experimental Approaches. *Photonics,* 8, 361. DOI:10.3390/photonics8090361
24. Pal, A., Shah, S., & Devi, S. (2009). Microwave-Assisted Synthesis of Silver Nanoparticles Using Ethanol as a Reducing Agent. *Materials Chemistry and Physics, 114*, 530–532, DOI:10.1016/j.matchemphys.2008.11.056
25. Das, R., Nath, S.S., Chakdar, D., Gope, G, & Bhattacharjee, R. (2010). Synthesis of Silver Nanoparticles and Their Optical Properties. *Journal of Experimental Nanoscience, 5*, 357–362. DOI:10.1080/17458080903583915
26. Dheyab, M.A., Aziz, A.A., Jameel, M.S., Khaniabadi, P.M., & Mehrdel, B. (2019). Mechanisms of Effective Gold Shell on Fe3O4 Core Nanoparticles Formation Using Sonochemistry Method. *Ultrasonics Sonochemistry, 64*, 209707397. DOI:10.1016/j.ultsonch.2019.104865
27. Fuentes-García, J.A. Santoyo-Salzar, J., Rangel-Cortes, E., Goya, G.F., Cardozo-Mata, V., & Pescador-Rojas, J.A. (2021). Effect of Ultrasonic Irradiation Power on Sonochemical Synthesis of Gold Nanoparticles. *Ultrasonics Sonochemistry,* 70*,* 105274, DOI:10.1016/j.ultsonch.2020.105274

sciendo

LATVIAN JOURNAL OF PHYSICS
AND TECHNICAL SCIENCES
2024, N 1

DOI: 10.2478/lpts-2024-0004

A PRACTICAL SOLUTION TO REDUCE INTERFERENCE FROM LED LIGHTS

J. Kallunki

Metropolia University of Applied Sciences,
Helsinki, FI-00079, FINLAND
E-mail: juha.kallunki@metropolia.fi

The study explores the detection of a harmful, wide-band interference signal, whose origin is a traditional desk LED (light-emitting diode) lamp. The interference signal was noticed on the sensitive solar spectrometer observing system, which was operating at a frequency range between 100 and 300 MHz. The interference signal was so strong and wide-band that it destroyed totally the solar observations. The study introduces two practical EMI (Electromagnetic Interference) reducing methods: ferrite cores and shielding (shielding effectiveness, S.E.). Their theoretical background is presented, and, in addition, these methods are tested in practice. The measurements and tests showed that even simple ferrite core was a very effective method to reduce interference effects. It is important that a suitable setup will be found: a single ferrite core cannot solve a whole problem. This interference problem is very demonstrative and it can be used in educational purposes at an undergraduate level at Metropolia University of Applied Sciences, Finland. This study reveals the fact that standard lamps, which are on the market, do not necessarily follow good EMC (Electromagnetic Compatibility) practices.

Keywords: *EMI reducing methods, LED lights, wide-band interference signals.*

1. INTRODUCTION

The radio frequency interference (RFI) is an increasing issue nowadays. Several electronic devices produce harmful interferences, including switching power supplies [1] and LED (light-emitting diode) based lighting solutions. They can, in the worst case, produce strong and wide-band interfering radio frequency transmission. Especially, Electromagnetic Compatibility (EMC) / Electromagnetic Interference (EMI) from LED lighting is a very common issue [2]. These problems may cause some interference issues to other sensitive electronic devices or radio frequency broadcasting and communications systems. The LED light usually consists of several small LED elements, which are connected to an array shape. LEDs are also driven by using PWM (Pulse Width Modulation). The PWM signals are sharp pulses, and they can generate wide frequency band interfering in signals up to several hundreds of MHz. The interfering signal moves along the cables. If these cables are not properly shielded, cables could act like a transmission antenna.

Such a harmful feature was found on the desk LED lamp (model: Airam Campus LED G23, 7.2 W) shown in Fig. 1. The lamp produces a wide band and strong interfering signal in the frequency range between 100 and 300 MHz. Figure 2 presents the radio spectrogram at a frequency range at 100 and 300 MHz. The interfering signal from the lamp is seen as a waving signal over the spectrum (Section 2 in Fig. 2). Figure 2 illustrates situations (Sections 1, 5 and 7) when the lamp is switched off, which confirms that an interfering signal is originated from the lamp. The monitoring system is designed to observe active solar events, especially transient phenomenon in the solar corona. The system has an omni-directional antenna with a gain of 7 dBi and pre-amplifier with a gain of 30 dB (with noise of around 1.5 dB). Figure 3 shows the receiving antenna. The distance between the desk lamp and the receiving antenna was approximately 15 m. The observing system is a single node of international e-Callisto solar observing network [3]. Radio frequency interference (RFI) is a major problem in the field of radio astronomy nowadays [4]–[6], especially at low frequency ranges (< 2000 MHz). The solar observations, in our situation, are not possible if the effect of the interfering signal cannot be reduced remarkably.

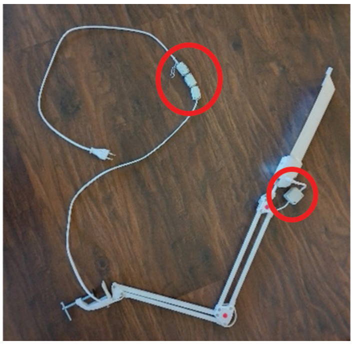

Fig. 1. The traditional, interfering desk lamp (model: Airam Campus LED G23, 7.2 W). The red circles indicate the location of ferrite cores.

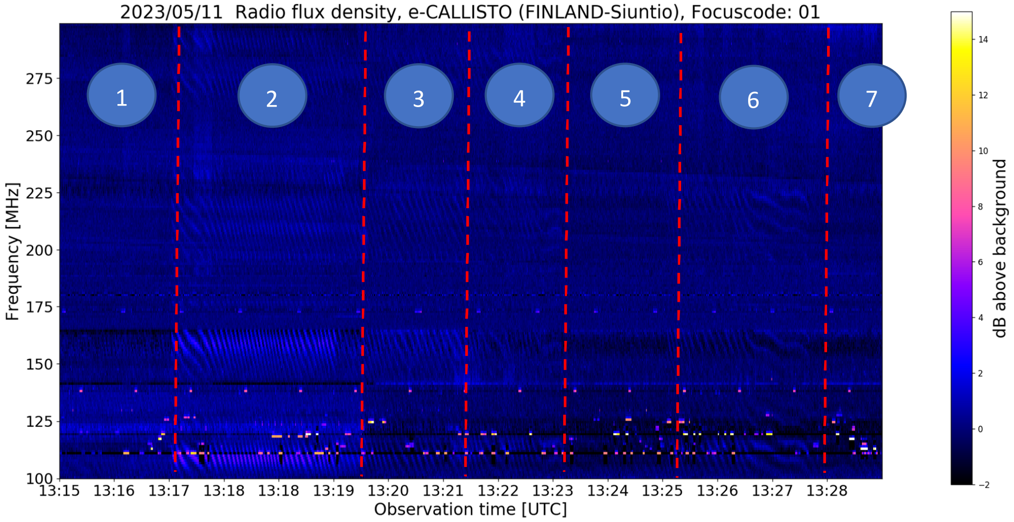

Fig. 2. The radio spectrogram at a frequency range between 100 and 300 MHz. The numbers indicate different sections (modes) under the test. In Table 1, modes are explained in detail.

Fig. 3. Omni-directional e-Callisto antenna in Siuntio, Finland. LNA (low-noise amplifier) is located under the eaves (marked with the red circle). The instrument has been operational since April 2023, and since that already tens of solar radio bursts have been detected.

The aim of this study is twofold: to find out a practical and feasible solution to decrease the effect of the interfering signal from the LED light and, secondly, to create a laboratory exercise about this topic to the undergraduate level students. This interference example is very suitable for hands-on exercise: it is practical and feasible. The students have possibility to try different solutions to decrease interference effects within a relatively short period of time, during two to three exercise hours.

Filtering and shielding solutions are obvious ways to reduce interference. Common mode ferrites, which are installed around the cable, are cost-effective solutions, and ferrites usually solve the problem partially. Another solution is to use EMC sleeve around the cable. The EMC cable sleeve prevents interfering transmission from cables. This solution is a way to realize shielding. This study only focuses on electromagnetic interference (radiative), and not, for instance, conductive interference (e.g., harmonics).

This article covers a theoretical overview of the common mode filtering and shielding effectiveness (S.E.), which is not usually taken into account when solving practical interference issues. In addition, the article demonstrates with measurements how much these solutions can improve interference situation in a specific interference case. Finally, future research areas are discussed in the article.

2. REDUCTION SOLUTIONS

2.1. Cable Ferrites

Cable ferrite is an easy and cost-effective solution to reduce interference effects. A ferrite cable core is designed to clean common mode noise (signal) generated from either a signal line or power cable. At radio frequencies, ferrite cores behave like an attenuator or a low-pass filter. Ferrites cause a back electromagnetic force (EMF) in the presence of a high-frequency signal. The installation is very easy and the cost of ferrites is low (< 10 €). They have usually a hinge; thus, ferrites can be installed afterwards in desired devices or cables. It is important to understand their impedance characteristic. The impedance characteristic informs about the suitable frequency range of ferrite, and in addition, its attenuation profile. Usually, the manufacturer gives two impedance values of ferrite with different frequencies (e.g., RRC-20-10-10-M, $Z = 50\,\Omega\,@\,25\,\mathrm{MHz}\,/\,Z = 105\,\Omega\,@\,100\,\mathrm{MHz}$). The impedance value is proportional to the attenuation:

$$A(db) = 20\log_{10}\left(\frac{Z_a + Z_f + Z_b}{Z_a + Z_b}\right), \tag{1}$$

where (Z_a) is the source impedance, (Z_b) is the load impedance and (Z_f) is the ferrite core impedance. If source impedance (Z_a) and load impedance (Z_b) are 50 Ω systems, attenuation (A) is 3.5 dB at 25 MHz and 6.2 dB at 100 MHz using parameters from the RRC-20-10-10-M ferrite. The greater the impedance, the higher the attenuation. There are three parameters, which affect ferrite core impedance: material type, number of turns and core size. The total impedance of the ferrite core (Z) is a sum of resistive and inductive components (2) [7].

$$\begin{gathered} Z = j\omega L_s + R_s = j\omega L_0(\mu' - j\mu'') \\ \omega = 2\pi f, \end{gathered} \tag{2}$$

where L_s is the series inductance, R_s is the series loss resistance, L_o is the air core inductance, f is the frequency, μ' is the real part of the material permeability and μ'' is the imaginary part of the material permeability. Furthermore, permeability (μ', μ'') can be defined as follows: [8]

$$\mu' = \frac{\ell L}{\mu_0 N^2 A}, \tag{3}$$

$$\mu'' = \frac{\ell R}{\mu_0 N^2 \omega A}, \tag{4}$$

where is the ferrite bead length, μ_0 is the permeability of the vacuum ($4\pi \times 10^{-7}$ H/m), A is the cross-sectional area of the toroidal core, ω is the angular frequency, R is the resistive component of the ferrite core, L is the inductance component of the cable ferrite, N is the number of turns (i.e., how many times cable travels through the core) and A is the effective cross-sectional area of the core. Figure 3 shows the schematic of the ferrite core.

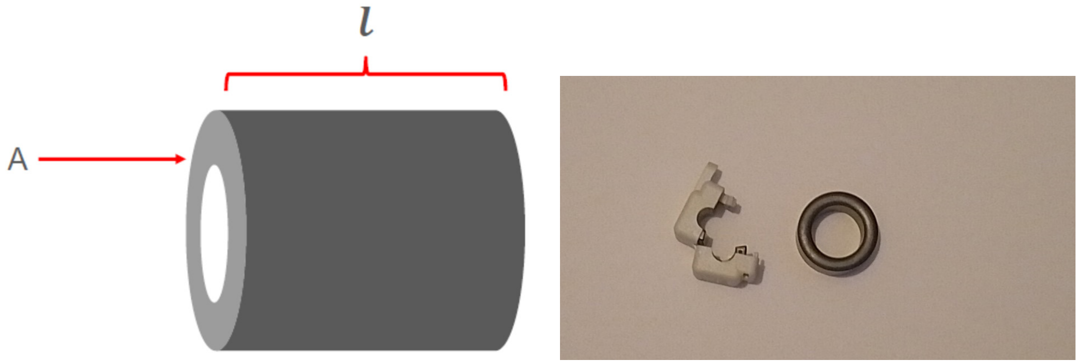

Fig. 4. The ferrite core. On the left, the schematic of the ferrite core is shown. On the right, different and common ferrite structures are presented.

According to the previous equations, the greater the length (ℓ) of the ferrite core cylinder, the higher the impedance. Thus, an increase in the core length is equivalent to the use of several ferrites together. In addition, it is concluded that the higher the frequency, the higher the impedance.

2.2. Shielding Effectiveness (S.E.)

Shielding is another way to reduce EMC/EMI effect. It is possible to shield in the device, which transmits interference. In addition, it is possible to use it on the device, which suffers in the transmission. Good results can be achieved even with a very thin shielding (< 1 mm). The complete shielding effectiveness (S.E.) consists of two parts: absorption and reflective losses (5), shown in Fig. 5.

$$S.E. = 20 \times \log \frac{\eta_0}{4\eta_s} + 20 \times \log e^{\frac{t}{\delta}} = R(dB) + A(dB), \tag{5}$$

where η_0 is the intrinsic impedance of free space (377 Ω), η_s is the intrinsic impedance of material, t is the material thickness, δ is the skin depth.

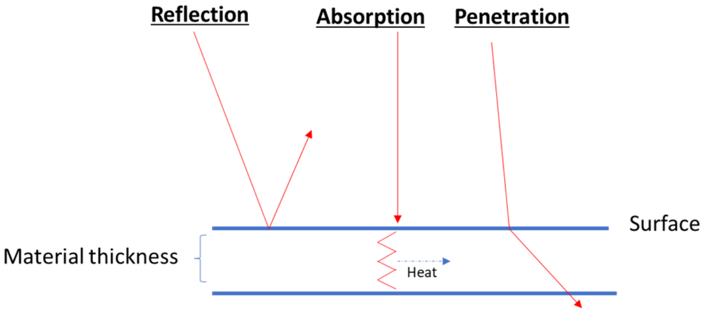

Fig. 5. A schematic representation of the EMI shielding mechanisms: reflection, absorption and penetration (modified from [9]). The total shielding effectiveness (S.E.) consists of reflection and absorption. The material type (conductivity of the material) and material thickness have great impact on the total shielding effectiveness.

The absorption loss can be estimated as follows:

$$A(dB) = 20 \times \log e^{\frac{t}{\delta}} \approx 8{,}7 \times \frac{t}{\delta}. \tag{6}$$

According to the previous equation, the thicker the material, the higher attenuation. The skin depth can be calculated as follows:

$$\delta = \frac{1}{\sqrt{\pi f \mu \sigma}}, \tag{7}$$

where f is the frequency, μ is the permeability of the vacuum ($4\pi \times 10^{-7}$ H/m), σ is the conductivity of the specific material. The reflective loss can be estimated as follows:

$$R(dB) = 20 \times \log \frac{\eta_0}{4\eta_s}. \tag{8}$$

The intrinsic impedance (η_s) of the specific material can be calculated as follows:

$$\eta_s = \sqrt{\frac{2\pi f \mu}{\sigma}}. \tag{9}$$

Finally, the total shielding effectiveness ($S.E.$) can be calculated as follows:

$$S.E. = R(dB) + A(dB). \tag{10}$$

For example, if we have aluminium foil with thickness of 1 μm, the total shielding effectiveness is 87.4 dB at 100 MHz. In the calculation, we used aluminium conductivity $\sigma_{al} = 3{,}8 \times 10^7$ S/m. This emphasises that the shielding is a very effective method to reduce EMI effect. However, any holes (such as a cable inlet) in the shielding can destroy the situation, and the total shielding effectiveness will be smaller.

3. RESULTS

Both ferrite and shielding were tested to find out their effect on the interference situation. In Fig. 2, seven numbers are marked, which indicate different interference and reducing method situations. In Table 1, they are explained in detail. Ferrites were installed in light power (230 Vac) cable and their positions are shown in Fig. 1 (red circles).

Table 1. Different Light ON-OFF-Status and Reduction/Mitigation Situation.
(The same numbers are seen in Fig. 2.)

No.	Status
1	Light off
2	Light on
3	Light on + a single ferrite (265 Ω at 100 MHz) on a power cable
4	Light on + four ferrites (1 x 265 Ω at 100 MHz + 3 x 247 Ω at 100 MHz) on a power cable
5	Light off
6	Light on + four ferrites (1 x 265 Ω at 100 MHz + 3 x 247 Ω at 100 MHz) on a power cable + lamp frame shielded with the aluminium foil
7	Light off

It is possible to notice that reducing methods affect the interference situation. A single ferrite (Fig. 2, Section 3) already reduces the interference effect, and adding even more ferrites, the situation is getting better (Fig. 2, Section 4) as it is expected. However, adding shielding around the lamp (Fig. 2, Section 6) did not improve the situation, and due to the lamp structure, we could not shield the full length of the cable. It is not possible to see major difference between Sections 4 and 6. In this situation, we can conclude that lamp power cable acts like an antenna and that should be shielded. The lamp power cable is unshielded, and the lamp has no earth wiring. Obvious improving method is to change a power cable to the shielded version of it. By adding more ferrites alone cannot solve the whole problem, even if it is a very effective method to reduce the interference problem. The used ferrites were all designed for low frequencies (< 200 MHz). Their impedance characteristic is not optimal anymore at higher frequencies (see Fig. 2). The waving interference signal is still visible at frequencies above 175 MHz even if the ferrites are installed.

4. CONCLUSIONS AND FUTURE RESEARCH AREAS

The study aimed at finding out a practical solution to reduce the interference effect. This aim was achieved partially. We found a simple solution, which was satisfactory. The lamp can be used when several ferrites are installed around the power cable. Without modifying the lamp structure anymore, it is hardly possible to achieve a better result. In addition, due to electric safety regulation, it is not allowed to perform any structural modifications to the lamp. It is important to keep this in mind. Clear reduction methods for minimizing unwanted interference are as follows:

- grounding;
- shielding in cables and all cases;
- filtering;
- designing aspects;
- opto-isolation.

These reducing methods are widely used. From the manufacturer's viewpoint, if these methods are taken into account completely, they bring some extra costs. However, with proper design, these extra costs are not very high. In this specific case, only filtering and shielding can be used to prevent EMI. A relatively new reducing method is the so-called spread spectrum technique. The idea is to spread a centralized energy at wider frequency bands. On the other hand, it means that EMI signal will spread on a larger band; thus, there should be fewer strong and harmful spikes in the spectrum. For instance, control methods of a new LED driver make this possible [10]. This might have potential to improve the interference problem.

The secondary aim of the study was to create a laboratory exercise about this topic to the undergraduate students. As mentioned above, the problem is practical, and it is suitable for the laboratory exercise. The situation could be repeated in the laboratory conditions and typical laboratory measurement devices could be used. The aim is to start to use this exercise as a laboratory work within the courses of measurement technology and EMC at the Helsinki University of Applied Sciences Metropolia, Finland [11]. This work is partly related to the project where we try to systemically develop EMC measurement and teaching facilities at Metropolia.

The solar radio spectrometer system is sensitive and it can detect very weak signals. In that sense, the case was special and, otherwise we could barely detect an interfering signal. However, it is not an unrealistic scenario that other sensitive electronics can also be disturbed. If the environment is sensitive to the radio interference, all the lamps should be tested carefully before making the final choice. Just CE (The Conformité Européene) marking does not alone guarantee that the device fulfils good EMC properties. In this case, we were not interested in the EMC minimum requirement level, so we did not perform any standardized measurements. Besides, when doing standardized EMC measurements, it is required to follow very carefully standards, which, for instance, provide strict regulations for the test methods, test equipment and test environment. The focus was to find a solution that low-frequency (< 300 MHz) solar observations could be made as well in the future.

REFERENCES

1. Li, L., & Zhang, X. (2022). EMI Analysis of a Switching Power Supply. *J. Phys.: Conf. Ser. 2246* 012048. doi: 10.1088/1742-6596/2246/1/012048
2. Wan, F., Cao, H., An, S., Feng, C., Hu, G., & Ge, J. (2016). Characterisation of Electromagnetic Interference from LED. *Electron. Lett., 52,* 143–144. https://doi.org/10.1049/el.2015.3358
3. e-Callisto. (n.d.). *International Network of Solar Radio Spectrometers, a Space Weather Instrument Array*. Available at https://www.e-callisto.org/index.html
4. Kallunki, J., Hase, H., & Zubko, N. (2023). Spectrum Management for the VLBI Global Observing System (VGOS) Observations. *International VLBI Service for Geodesy and Astrometry 2022 General Meeting Proceedings*, 14–18.

5. Kallunki, J., Bezrukovs, V., Madkour, W., & Kirves, P. (2022). Importance of Spectrum Management in Radio Astronomy. *Latvian Journal of Physics and Technical Sciences, 59*, 30–38. doi:10.2478/lpts-2022-0022.
6. Kallunki, J., Bezrukov, D., Avotins, V., & Bleiders, M. (2019). Particularly Low-Cost Portable Radio Frequency Interference Monitoring System. *International Journal of Electromagnetic (IJEL), 2* (1), 1–7. Available at https://airccse.com/ijel/papers/2119ijel01.pd
7. Parker, R. (2007). *75-material for Low-Frequency EMI Suppression Demystified*. (White paper). Fair-Rite Products Corp. Available at https://www.dextermag.com/wp-content/uploads/2017/03/Dexter_Fair-Rite_75-material_WhitePaper.pdf
8. Suarez, A., Victoria, J., Alcarria, A., Torres, J., Martinez, P.A., Martos, J., … & Muetsch, S. (2018). Characterization of Different Cable Ferrite Materials to Reduce the Electromagnetic Noise in the 2-150 kHz Frequency Range. *Materials (Basel), 11* (2), 174. doi: 10.3390/ma11020174.
9. Kruželák, J., Kvasničáková, A., Hložeková, K., & Hudec, I. (2021). Progress in Polymers and Polymer Composites Used as Efficient Materials for EMI Shielding. *Nanoscale Adv., 3*, 123. doi: 10.1039/d0na00760a
10. Hariyawan, M., Y., Hidayat, R., & Firmansyah, E. (2016). An Experimental Study of Conducted EMI Mitigation on the LED Driver Using Spread Spectrum Technique. *International Journal of Electronics And Telecommunications, 62* (3), 293–299.
11. Metropolia University of Applied Sciences. (n.d.). Available at https://www.metropolia.fi/en

LATVIAN JOURNAL OF PHYSICS
AND TECHNICAL SCIENCES
2024, N 1

DOI: 10.2478/lpts-2024-0005

COMPENSATION OF ACCURACY ERROR FOR TIME INTERVAL MEASUREMENTS

V. Bespal’ko[1], A. Litvinenko[2], V. Stepanovs[1],
V. Kurtenoks[1], V. Smetska[1,2], V. Lapkovskis[1,2]*

[1]Eventech Ltd.,
3 Pulka Str., Riga, LV-1007, LATVIA
[2]Riga Technical University, Institute of Radio Electronics,
12 Azenes Str., Riga, LV-1048 LATVIA
*e-mail: vjaceslavs.lapkovskis@rtu.lv

A method of accuracy error compensation for the time interval is examined, allowing to decrease the dependence of accuracy error on the duration of measured intervals and minimising the influence of destabilising factors – ambient temperature changes and the initial deviation of the meter clock generator frequency from the nominal value. The compensation method is based on a calibration procedure that measures precise time intervals under conditions of changing ambient temperature. Then the dependence of the accuracy error on temperature for a particular meter is recorded. Based on these data, a correction table is compiled containing correction factors and temperature values at which these factors were determined. Under real measurement conditions, the correction factor corresponding to the current temperature is determined from the table for measured result correction. The table with correction factor values could be stored in the memory of the meter or processing computer. Experimental verification of the method showed that applying a correction for a meter with a standard XO class clock generator (certificated instability of ±50 ppm) could obtain an equivalent clock generator instability of ±0.15 ppm. The application of the method is efficient in cases where the use of high-end clocking to ensure the required measurement accuracy is not economically feasible.

Keywords: *Accuracy error compensation, clock generator, correction of measurement results, measurement of time intervals.*

1. INTRODUCTION

Time measurements (time-to-digital conversion) [1]–[4] have always belonged to the class of the most demanded measurements since it is reasonable to reduce measurements of many heterogeneous physical quantities to time measurements. As modern methods and instruments for measuring time provide very high accuracy [5], these technologies are in demand in a wide range of fields and industries [6], [7]. The most commonly used time measurements are measurements of time intervals (TI) between the start and stop input signals [8], [9]. For a significant part of the experiments, the object of investigation is the time relations between initialising and secondary events [10], [11].

In the analysis of measurement errors of time intervals, we assume that the result A_i of the i-th measurement is, in general, a random variable and can be represented as a sum of the measured quantity T_i and the absolute error of its measurement a_i:

$$A_i = T_i + a_i\,.$$

The absolute measurement error a_i can, in turn, be represented as the sum of the random Δ_{ir}, accuracy Δ_{is} and offset Δ_c components of the total error [12], therefore:

$$A_i = T_i + a_i = T_i + \Delta_{ir} + \Delta_{is} + \Delta_c. \tag{1}$$

The random error (or precision error) Δ_{ir} has an unpredictable value and represents the scatter of the measurement results due to the influence of noise of different origin.

The accuracy error is determined by the repeatability of its value from measurement to measurement. However, the value of this error Δ_{is} itself depends on several parameters. The characteristic of the accuracy error in TI measurement is its multiplicative character, i.e., the value of Δ_{is} is proportional to the duration of the measured TI.

The offset error is determined by the difference between the delays of the start and stop channels and is additive. Its value Δ_c is offset for a particular meter. The offset error can be determined and used to correct the measurement results accordingly.

Let us suppose that the task is to test a meter. In that case, the value of T_i in (1) is generally unknown since the source (generator) of input signals possesses its errors (Accuracy, Offset, Jitter). Ti can be represented as the sum of the generator set value T_g, generator accuracy error Δ_{isg}, generator constant error Δ_{cg} and jitter of the TI generator Δ_{irg}. Therefore, the general equation of the measurement result is as follows:

$$A_i = T_i + a_i = T_g + \Delta_{irg} + \Delta_{isg} + \Delta_{cg} + \Delta_{ir} + \Delta_{is} + \Delta_c. \tag{2}$$

A graphical interpretation of the generation and measurement errors is illustrated in Fig. 1.

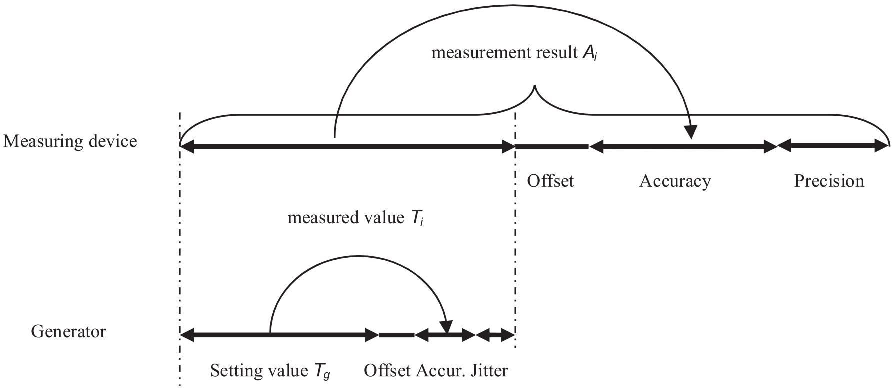

Fig. 1. Graphical interpretation of the generation and measurement errors of the time intervals.

The accuracy error Δ_{is} in the TI measurement is determined by the stability level of the clock generator (CG) of the meter and is caused by the fact that the period F of the CG differs from the nominal value F_0 by τ. The value of τ is not constant and depends on four factors: changes in ambient temperature, the value of the initial deviation from F_0, variations in the generator supply voltage and ageing of its components.

In the specifications of a CG, the maximum value of its relative stability is K_{max}, defined as ratio $K_{max}=\pm\tau_{max}/F_0$, where τ_{max} takes into account all destabilising factors. According to the methods of minimising the influence of destabilising factors, CGs are divided into stability classes [13], [14]: standard XO (Crystal Oscillator), thermo-compensated TCXO (Temperature Compensated Crystal Oscillators), thermo-stated OCXO (Oven Controlled Crystal Oscillators), microprocessor-corrected MCXO (Microprocessor Corrected Crystal Oscillator), and atomic standards.

Reducing the accuracy error is relatively easy to achieve by using high-end CG in the meter. However, for specific applications (e.g., space electronics), such a solution is not always feasible due to the high cost of high-class CGs, as the main cost component of space-level CGs is the testing procedure. In this paper, the problem of significant reduction of the accuracy error without increasing the CG class of the TI meter is solved.

2. ESTIMATION OF ACCURACY ERROR

When measuring time intervals, the result of measurement A_i is proportional to the period of CG F, which determines the multiplicative nature of the accuracy error, and its value Δ_s increases proportionally to the duration of measured TI. The maximum value of accuracy error Δ_{smax} is usually the parameter of the meter, which can be estimated based on the certificate value K_{max} for the applied CG and A_{max} value, corresponding to the upper limit of the range of measured TI durations: $\Delta_{smax} = K_{max} \cdot A_{max}$.

The experience shows that the K_{max} value of a particular CG for the specific temperature conditions of its application can be much less than the value taken from its specification data. Respectively, the real value of Δ_{smax} can also be several times less.

Therefore, the first step in reducing the accuracy error is to estimate the Δ_{smax} value of a particular CG meter.

Evaluation of Δ_{smax} of a particular TI meter is based on measurement and accumulation of an array *[A]* of *n* results of the TI measurement (Fig. 2) for the case of measuring input TI of maximum duration T_{gmax} when the ambient temperature $t°$ changes in the operating temperature range of the meter. Based on (2), it can be assumed that the average value of the array of measurement results at temperature $t°$ will be:

$$\bar{A}_{t^\circ max} = T_{g\,max} + \Delta_{cg} + \Delta_{cg} + \Delta_{t^\circ s} + \Delta_c . \quad (3)$$

In this case, we assume zero values of the meter's random error and the TI oscillator's jitter. The influence of the accuracy error of the generator Δ_{sg} included in this expression can be neglected if the stability of its CG is 1–2 classes higher than the CG stability of the TI meter under study. Thus, Fig. 2 shows the use of an external OCXO (reference oscillator). In this case, Expression (3) is simplified:

$$\bar{A}_{t^\circ max} = T_{g\,max} + \Delta_{cg} + \Delta_{t^\circ s} + \Delta_c . \quad (4)$$

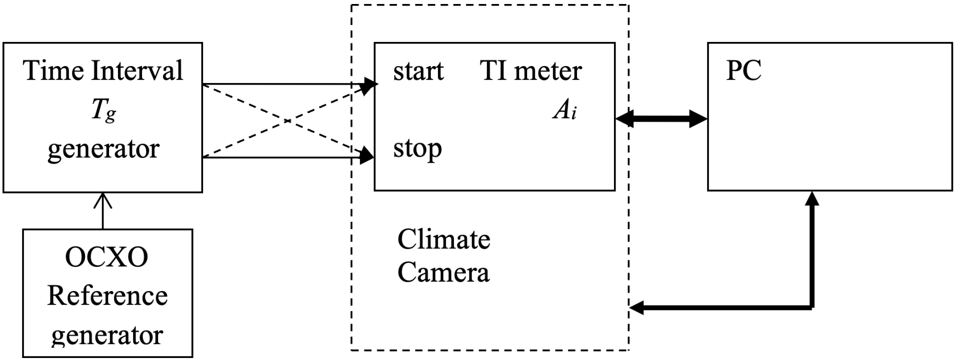

Fig. 2. Flow chart of the systematic and constant error estimation of the TI meter.

Equation (4) used to evaluate the accuracy error $\Delta_{t°c}$ is complicated due to the presence of unknown error constants Δ_{cg} and Δ_c in the expression. The value of Δ_c is determined by the difference in delays for the start and stop inputs of the TI meter. In turn, Δ_{cg} is determined by the difference in delays in the TI meter start and stop signal generation circuitry and the difference in the lengths of the connection wires.

It is possible to estimate the values of Δ_{cg} and Δ_c when two conditions are met. Firstly, the TI must be measured with a minimum duration of T_{gmin}, which allows for omitting the accuracy errors of the generator Δ_{sg} and the measurer Δ_s, then:

$$\bar{A}_{min} = T_{g\,min} + \Delta_{cg} + \Delta_c .$$

Secondly, additional measurements are required when the wires are cross-connected to the meter inputs (shown in dashed in Fig. 2), and the sign of inter-channel delay of the TI generator is changed. In this case, a system of equations can be formulated:

$$\bar{A}_{1\,min} = 2T_{g\,min} + \Delta_{cg} + \Delta_c ;$$

$$\bar{A}_{2\,min} = 2T_{g\,min} - \Delta_{cg} + \Delta_c .$$

This implies that:

$$\Delta_{cg} = \frac{\bar{A}_{1max} - \bar{A}_{2max}}{2};$$

$$\Delta_c = \frac{\bar{A}_{1max} + \bar{A}_{2max} - 2T_{g\,min}}{2}.$$

Estimation of the error constant of the meter relative to its inputs Δ_c is an independent value, but, at the same time, it provides the capability for estimation of $\Delta_{t^\circ s}$:

$$\Delta_{t^\circ s} = \bar{A} - \left(T_{g\,max} + \Delta_{cg} + \Delta_c\right) = \frac{1}{n}\sum_{i=1}^{n} A_{t^\circ i} - \left(T_{g\,max} + \Delta_{cg} + \Delta_c\right). \quad (5)$$

While testing the meter in a climate chamber within the meter's operating temperature range (Fig. 2), a dependence of $\Delta_{t^\circ s}$ on ambient temperature changes t° can be derived by TI measurement of maximum duration T_{gmax}. The graphical representation provides a capability to estimate the value of Δ_{smax} for a particular TI meter and the actual stability of its clock generator $K_{max}=\pm\Delta_{smax}/T_{gmax}$.

Figure 3 shows an example of the plot of change of Δ_s as a function of temperature for a TI meter with a standard XO class clock generator (according to its specification $K_{max}=\pm 50$ ppm). The dependence character in the operating temperature range of the meter (- 40 °C ÷ +60 °C) is of a pronounced non-linear nature and corresponds to the frequency-temperature characteristics of quartz AT-slice plates.

Based on Fig. 3, $\Delta_{smax}=740$ ps and $T_{gmax}=134$ µs; hence, the estimate of $K_{max}=\pm 740\cdot 10^{-12}/134\cdot 10^{-6}= 5.5\cdot 10^{-6}=\pm 5.5$ ppm. The estimation of K_{max} obtained in this way is underestimated since it does not take into account the influence of instability of the generator supply voltage and the ageing of its components. Nevertheless, the difference between the specification listed and the actual component's parameter values is sufficient.

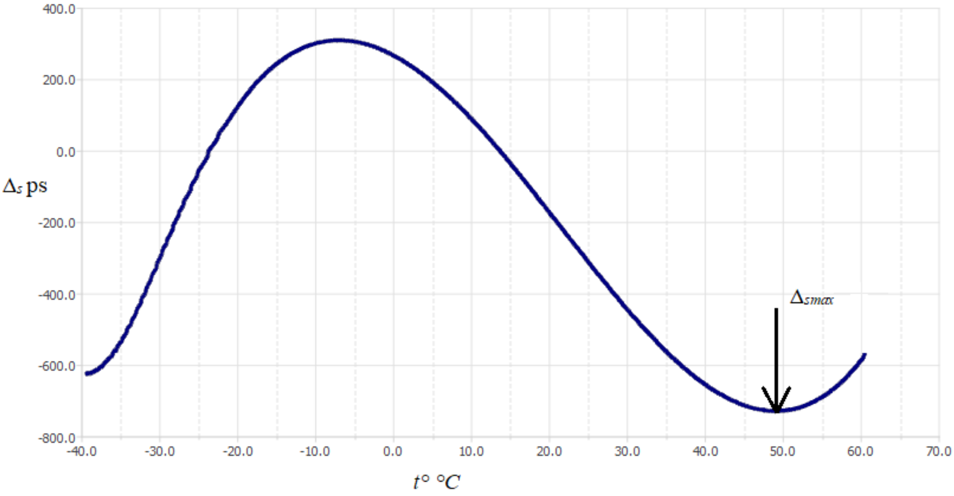

Fig. 3. The temperature dependence Δ_s for an XO standard class TI meter when measuring TI with a duration of $T_{gmax}=134$ µs.

3. COMPENSATION FOR ACCURACY ERROR

The investigation of the dependence of the accuracy error value Δ_s on the temperature for a particular CG provides the capability to perform a procedure for offsetting the influence of the accuracy error on the measurement result.

The compensation procedure is based on a special calibration, during which a series of high-precision TI measurements are carried out under changing ambient temperature $t°$. This is done by determining the average values of the TI measurement $\bar{A}_{t°}$ and the accuracy error $\Delta_{t°s}$ for the current temperature $t°$ according to (5). The correction factors $\mathrm{K}_{t°}=\Delta_{t°s}/\bar{\mathrm{A}}_{t°}$ and the corresponding temperature calculated from these data are recorded as a table of $\mathrm{K}_{t°}$ and $t°$ values in the memory of the meter or processing computer.

Considering the non-linear nature of the relationship between the accuracy error and temperature (Fig. 3), the choice of a table to record the relationship between the correction factors and temperature is the simplest method, although it requires memory resources.

Several conditions have to be met during calibration: the CG class of the TI generator must be higher than the CG class of the measured (compensated) meter, the results of the calibration measurements must be averaged to increase the accuracy of the table, and the T_{gmax} value must correspond to the maximum working range of the TI durations to be measured.

In general, calibration should be carried out under the real conditions of the meter's use or its equivalent. For example, if we are talking about space applications, then calibration must be carried out under thermo-vacuum conditions.

To implement the procedure for compensating for the accuracy error under actual measurement conditions, it is essential to monitor the current temperature $t°$. The algorithm for compensation of the *i*-th measurement result consists of extracting from the table the $\mathrm{K}_{t°}$ coefficient corresponding to the temperature $t°$ at the time of measurement and calculating the compensated measurement result $\mathrm{A}_{t°i}$: $com\mathrm{A}_{t°i}=\mathrm{A}_{t°i}(1-K_{t°})$.

In a general case, the measurement result $\mathrm{A}_{t°i}$ contains both an accuracy error and a constant error Δ_c, so $\mathrm{comA}_{t°i}=(\mathrm{A}_{t°i}-\Delta_c)(1-\mathrm{K}_{t°})$. Figure 4 represents the dependence of the accuracy error Δ_s on the temperature after the compensation of the accuracy error shown in Fig. 3. The value of Δ_{smax} decreased from 740 ps to 20 ps, and the equivalent stability of CG, in this case, reached a value of ±0.15 ppm.

The compensation procedure also has its limitations since it does not consider the influence of instability of CG supply voltage and the ageing of its components.

As in the proposed solution, a variant of accuracy error minimisation implying a pre-calibration procedure is presented in [15]. This option is based not on the correction of measurement results but on microprocessor correction of frequency of VCXO class CG, the frequency of which is controlled by DAC voltage.

The microprocessor performs the calibration by the user. As a result of this procedure, the coefficients of the 4th-degree polynomial are determined and stored. These coefficients are used to calculate the DAC codes, which compensate the VCXO frequency deviation for the current temperature value $t°$. The CGs based on this principle belong to the CCXO (Coefficient Corrected Oscillator) class and can ensure the stability of the CG at the level of 0.1÷0.3 ppb. In its application, there is no need to manually correct measurement results, but the cost of such CGs is high, and at this time, it is not manufactured for the space-level ready version.

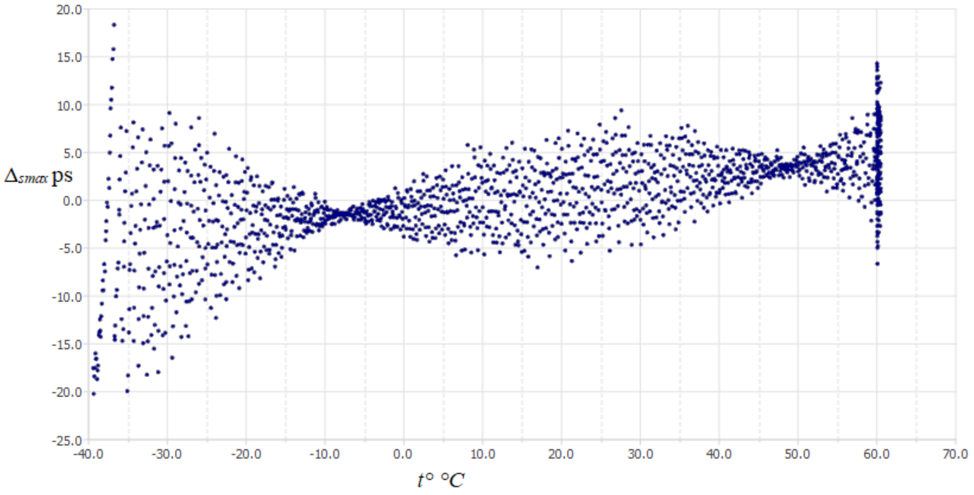

Fig. 4. Dependence of the accuracy error value Δs to the temperature after compensation.

4. CONCLUSIONS

The accuracy error at measuring time intervals (TI) is determined by the relative stability of the clock generator (CG) used in a meter and the duration of the measured time interval. The discussed method of accuracy error compensation eliminates the dependence of accuracy error on the duration of measured TI. It reduces to a minimum the influence of such destabilising factors as changes in ambient temperature and initial deviation of the clock frequency from its nominal value.

To implement the compensation method, three procedures have been developed: a procedure for registering an accuracy error, a calibration procedure in which a correction table is generated, and a procedure for correcting measurement results in real conditions of the meter's application. The main expenditures of implementing the method consist primarily in correctly conducting the meter's calibration, and hardware support for temperature monitoring and performing relatively straightforward computational operations is also required. The main costs of the method implementation primarily consider the correct calibration of the meter, as well as the required hardware support for temperature monitoring and relatively simple computational operation performance.

Experimental validation of the method demonstrated that an equivalent instability of ±0.15 ppm could be achieved for a standard class XO meter (specification instability of ±50 ppm), which reduced the accuracy error to the equivalent degree. The accuracy error compensation procedure has its limitations related to the replicability of the field conditions in which the calibration procedure has been performed.

Implementation of the described method of systematic error compensation has limited feasibility in terrestrial applications, when a given level of systematic error in time interval measurement can be obtained without much cost by simple selection of the required clock class. In space electronics, replacement of a complex high class clock by a simple standard XO class clock not only reduces significantly the cost of electronics, but in combination with simple computational operations, performed by an on-board computer, it also increases manifold the reliability of the CG. Modern capabilities for resetting the onboard computer increase another important parameter for space electronics – the survivability of the CG.

Systematic error compensation procedure has its limitations related to reproducing real conditions of instrument application during the calibration procedure. However, the pre-flight preparation of the electronics includes a mandatory TVC (Thermal Vacuum Cycle) procedure, during which calibration is possible. Also, space electronics are equipped with obligatory hardware support to monitor temperature, voltage and power supply levels to ensure reliability of measurement results. The above considerations make it possible to achieve a good balance between the cost of the method and its effectiveness.

ACKNOWLEDGEMENTS

The research has been supported by the European Regional Development Fund, project no. 1.1.1.1/20/A/104 “Multichannel Picosecond Precision Time-Tag System with Amplitude Measurements Capability for Satellite Laser Ranging”.

REFERENCES

1. Maichen, W. (2006). *Digital Timing Measurements: From Scopes and Probes to Timing and Jitter* (vol. 33). Springer US. https://doi.org/10.1007/978-0-387-31419-8
2. Alahdab, S., Mäntyniemi, A., & Kostamovaara, J. (2013). Review of a Time-to-Digital Converter (TDC) Based on Cyclic Time Domain Successive Approximation Interpolator Method with sub-ps-level Resolution. *2013 IEEE Nordic-Mediterranean Workshop on Time-to-Digital Converters (NoMe TDC)*, 1–5. https://doi.org/10.1109/NoMeTDC.2013.6658237
3. Tancock, S., Rarity, J., & Dahnoun, N. (2021). Developments in Time-to-Digital Converters during 2020. *2021 7th International Conference on Event-Based Control, Communication, and Signal Processing (EBCCSP)*, 1–5. https://doi.org/10.1109/EBCCSP53293.2021.9502397
4. El-Hadbi, A., Elissati, O., & Fesquet, L. (2019). Time-to-Digital Converters: A Literature Review and New Perspectives. *2019 5th International Conference on Event-Based Control, Communication, and Signal Processing (EBCCSP)*, 1–8. https://doi.org/10.1109/EBCCSP.2019.8836857
5. Johansson, S. (2021). Parallel, Multi-Channel Frequency & Time Measurements, with Picosecond Resolution. *Sensors & Transducers*, *254* (7), 1–9.
6. Gan, Q., Wang, W., Liu, Y., & Liu, W. (2022). Study on the High Precision Time-Interval Measurement System Based on FPGA and TDC_GP22. *9th International Symposium on Test Automation & Instrumentation (ISTAI 2022)*, 380–382. https://doi.org/10.1049/icp.2022.3253

7. Li, X. (2011). The Application Research Based on High-Precision's Measurement Method of Time Interval. *2011 International Conference on Multimedia Technology*, 3713–3715. https://doi.org/10.1109/ICMT.2011.6002696
8. Szplet, R., Kwiatkowski, P., Jachna, Z., & Różyc, K. (2016). An Eight-Channel 4.5-ps Precision Timestamps-Based Time Interval Counter in FPGA Chip. *IEEE Transactions on Instrumentation and Measurement*, *65* (9), 2088–2100. https://doi.org/10.1109/TIM.2016.2564038
9. Zhao, J., Zhao, Z., & Fu, L. (2017). Research on the High Resolution Precision Time-interval Measurement Methods. *Procedia Engineering*, *174*, 1257–1261. https://doi.org/10.1016/j.proeng.2017.01.298
10. Raina, H., Sankannawar, P., Sawant, V., & More, J. (2022). Implementation of Multi-Channel Time-to-Digital Converter using FPGA. *2022 2nd International Conference on Intelligent Technologies (CONIT)*, 1–6. https://doi.org/10.1109/CONIT55038.2022.9847891
11. Nissinen, J., Nissinen, I., & Kostamovaara, J. (2009). Integrated Receiver Including Both Receiver Channel and TDC for a Pulsed Time-of-Flight Laser Rangefinder with cm-Level Accuracy. *IEEE Journal of Solid-State Circuits*, *44* (5), 1486–1497. https://doi.org/10.1109/JSSC.2009.2017006
12. Crowder, S., Delker, C., Forrest, E., & Martin, N. (2020). *Introduction to Statistics in Metrology*. Springer Nature.
13. Rutkowski, R. (n.d.). *Crystal Oscillators: The Beginners Guide (OCXO, TCXO, VCXO, Clocks)*. Available at https://blog.bliley.com/quartz-crystal-oscillators-guide-ocxo-tcxo-vcxo-clocks
14. *Quartz Crystal Cuts: AT, BT, SC, CT. Electronics Notes*. (n.d.). Available at https://www.electronics-notes.com/articles/electronic_components/quartz-crystal-xtal/crystal-resonator-cuts-at-bt-sc-ct.php
15. Vectron International. (2014). *Application Note. Coefficient Corrected Oscillator—CCXO*. Available at https://www.vectron.com/products/literature_library/Coefficient_Corrected_Oscillator_Application_Note.pdf

LATVIAN JOURNAL OF PHYSICS
AND TECHNICAL SCIENCES
2024, N 1

DOI: 10.2478/lpts-2024-0006

CHARGE ASSESSMENT FOR NITRATE-BASED SALT AS A PHASE CHANGE MATERIAL FOR A MEDIUM-TEMPERATURE LATENT STORAGE TANK

Ismail, Y. I. Widodo, R. A. Rahman*

Department of Mechanical Engineering,
Faculty of Engineering, Universitas Pancasila,
Srengseng Sawah. Jagakarsa 12640, DKI Jakarta, INDONESIA
*e-mail: reza.a@univpancasila.ac.id

The present study assesses the heat characteristic of the nitrate-salt mixture as a phase change material (PCM) for a medium-temperature latent storage system (LSS). Two binary and ternary mixtures are evaluated, which demonstrate different thermal behaviour. The highest melting and latent heat capacity is obtained by KNO_3(0.4)/$NaNO_3$(0.6) at 223.8 °C and 161.5 J/g. However, it has a higher supercooling degree with a partial phase transition between 217.6 °C and 251.5 °C, making it unfeasible for a medium-temperature LSS tank. The ternary mixture (TM) with $NaNO_2$(0.4)/KNO_2(0.53)/$NaNO_3$(0.7) demonstrates a stable phase transition with minimum partial phase transition (22.1 °C) and suitable heat of fusion (98.1 J/g). Further evaluation through static thermal profiling demonstrates that the TM has a notable performance during solid-sensible charge with a charge level indicator (CLI) around 45.3 %–49.1 %. The TM can be charged up to 85.7 % until the end stage of the phase transition. It promotes a better storage capacity with suitable performance since the system can be charged effectively at a suitable temperature range (< 160 °C) for various applications. The micrograph observation indicates some dispersed particles and local agglomeration, which makes phase stabilization as an advantageous method to promote a stable phase change process. The TM can be considered a suitable PCM for a medium-temperature LSS tank that allows for a better solar thermal renewable system operation.

Keywords: *Charge, latent heat, molten salt, nitrate based, solar thermal.*

1. INTRODUCTION

Advanced development of the energy sector from renewable sources becomes mandatory. It helps reduce the risk of energy crisis and mitigate climate change. Sustainable effort in the wind energy sector leads to a significant improvement in capacity, which reduces energy costs [1]. Combining the renewable sector with wind and solar energy provides positive outcomes, which make the system applicable in various sectors. It is possible to couple the system with the help of thermal energy storage (TES), which promotes a better dispatchability and operational aspect in the energy system [2]–[4].

Storing the heat energy through TES can be considered a cost-effective method for a thermal system. High consumption in heating application, such as solar water [5] and air heater [6], leads to enormous fuel consumption. It can be minimized by coupling the solar heater [7] system with TES, which allows the system to store excessive heat during the daytime and release heat at night [8]. The integrated solar thermal and TES system reduces the specific energy cost, which motivates researchers to improve the technology further, particularly for the TES system [9]–[11].

The high storage capacity for the TES system can be obtained by utilising a phase change material (PCM) through a latent storage system (LSS) tank [12]. The LSS provides a higher energy density, reducing the specific tank size and storing a higher quantity of heat energy [13]. The LSS system for water and air heater generally uses low-temperature PCM, which mainly comes from fatty acid [14], hydrocarbon wax [15], and natural wax [16]. The low thermal response for the LSS tank is overcome by using solid additives [17], a high surface area heat exchanger [18], and nano-enhanced working fluid [19]. The effort allows for building a desirable LSS tank. However, there is one significant drawback to the system. It uses low-temperature PCM, which limits the operation below 100 °C due to the melting temperature of the organic PCM commonly ranging between 50–68 °C.

The melting temperature for the LSS tank is a crucial aspect. The TES system uses the basic principle of heat transfer, which requires a temperature gradient between the storage tank and the thermal load [20]–[22]. Thus, a higher melting temperature of the PCM is desirable to promote a better operation of the LSS tank. The alternative PCM that can be considered the ideal candidate for a medium-temperature LSS tank is a nitrate-based salt mixture [23]. The melting temperature for the binary mixture (BM, around 240 °C) and ternary mixture (BM, around 140 °C) are considered high enough for application in solar air and water heater systems [24]. Salt mixture is exceptionally cheap, has suitable thermal capacity, and is stable in the liquid phase. It makes the mixture as an alternative option for the medium-temperature storage tank.

The mixture is applied as heat transport fluid for the concentrated solar power (CSP) system, which requires further adjustment to protect it from thermal decomposition [25]. Several studies have been performed to promote a stable phase behaviour using porous-ceramic [26], metal chlorides [27], and mesoporous silica [28]. However, the effort is focused on high-temperature applications (> 450 °C). For medium-temperature applications, the salt mixture seems relatively safe in its present form. Moreover, stabilization with high-density polymer [29] to build an immiscible LSS tank [30] can be conducted without complex and excess material modification. Thus, the salt mixture can be taken as the ideal candidate for a medium-temperature LSS tank.

The present study is motivated by the need to improve the LSS tank for medium-temperature applications to maximise the role and operation of the solar thermal system. With a better LSS tank, the system can fully operate from solar energy and can be improved to accommodate various heating applications. Thus, the study is conducted to evaluate the salt mixture in a medium-temperature LSS tank. The paper focuses on thermal characteristics and material aspects of the salt mixture to demonstrate that a salt mixture is suitable for LSS tanks. The finding is expected to provide a new perspective for utilising the salt mixture for medium-temperature LSS tanks, which may lead to an advanced LSS system for solar water systems.

2. MATERIALS AND METHOD

Two binary (BM) and ternary mixtures (TM) were prepared with the ratio as presented in Table 1. The raw materials were purchased from a local supplier that had industrial grade. Each raw material was preheated to remove the water content. The heating process was performed at 150 °C and 200 °C for 3 and 5 hours, respectively. The sample was mixed in the sealed argon atmosphere (glove box) to protect it from environmental moisture contamination. The primary thermal properties of each sample were evaluated through the calorimetry method.

Table 1. The Composition of the Salt Mixture

Ratio (Weight %)			**Identifier**
KNO_3	**$NaNO_3$**	**$NaNO_2$**	
40	60	-	BM_A
-	50	50	BM_B
53	7	40	TM_A
53	40	7	TM_B

Static thermal profiling (STP) was performed for each sample to evaluate its charging characteristic. Samples were heated by two electric heaters regulated with a power regulator (Fig. 1a). The heating rate was set at 100 J/s and monitored by an energy meter. Four temperature measurements were set within the sample chamber (Fig. 1b). The container was made of stainless steel and covered with a thermal insulator (glass wool). The mass of the sample for the STP process was 500 g. The high sample content is expected to understand the equilibrium profile during the charging process, which is similar to the LSS tank.

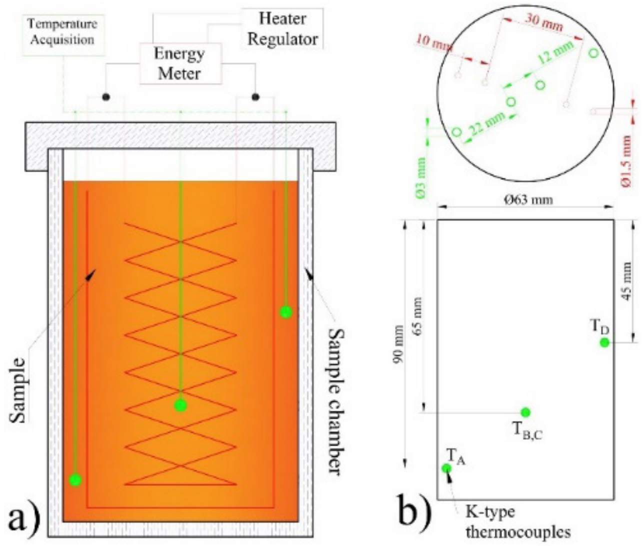

Fig. 1. Static thermal processing: (a) Detailed STP process and (b) the dimension of the apparatus / measurement positions.

3. RESULTS AND DISCUSSION

The key parameter for the LSS tank is the thermal properties of the PCM, which are related to its phase transition temperature and heat of fusion. Both parameters are essential for determining proper operation in the LSS tank. The BM salt has a higher phase transition temperature than the TM salt (Fig. 2a). The eutectic profile for BM can reach the highest melting temperature for each salt constituent, while the ternary profile for TM allows it to achieve the lowest melting temperature, particularly for TM_A. Thus, the designation of SM can be adjusted for specific purposes in the LSS tank.

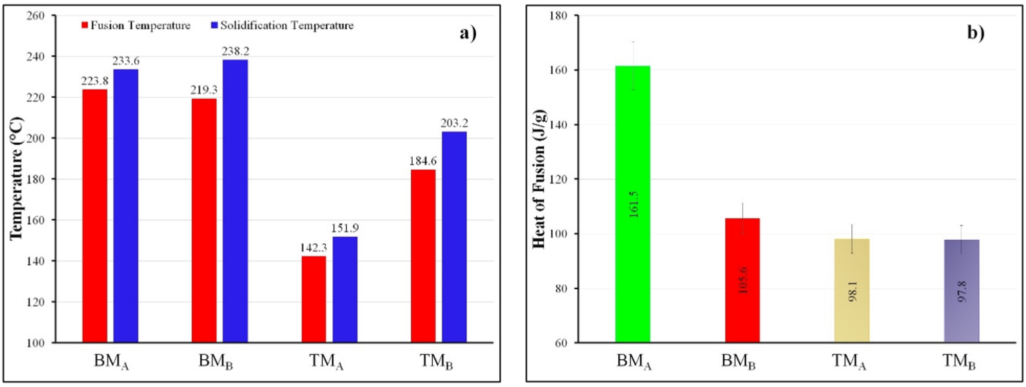

Fig. 2. Parameters of the LSS tank: (a) The latent heat capacity and (b) phase transition temperature.

The solidification temperature for all mixtures is higher than its melting temperature. It implies that the supercooling degree takes place. The highest degree is obtained for BM_B and TM_B with more than 18 °C. The presence of $NaNO_2$ in both samples lead to rapid solidification, which can be affected by the kinetic solidification rate for nitrites. It makes stabilizing both samples essential to reduce the high nucleation rate during solidification [31]–[33]. Interestingly, BM_A and TM_A experience supercooling phenomena at lower values (< 10 °C). The absence of nitrite for BM_A maintains sufficient solidification kinetic for the eutectic mixture and the higher nitrate content for the TM_A reduces the rapid heat releasement, minimising the supercooling effect.

The highest thermal capacity is achieved by BM_A, which is an eutectic mixture of KNO_3 and $NaNO_3$. The high thermal capacity is favourable for the LSS system [34]. The presence of nitrites reduces the latent heat of fusion for BM_B and TM by around 34.6 % and 39.4 %, respectively. Even though nitrite has the highest heat of fusion among nitrate and potassium nitrate [35], the binary and ternary mixtures promote a different melting behaviour. It is followed by a complex endothermic process that disrupts the total heat of fusion in the given melting temperature. However, the presence of nitrite decreases the melting temperature of the mixture so that proper adjustment can be made for the LSS tank.

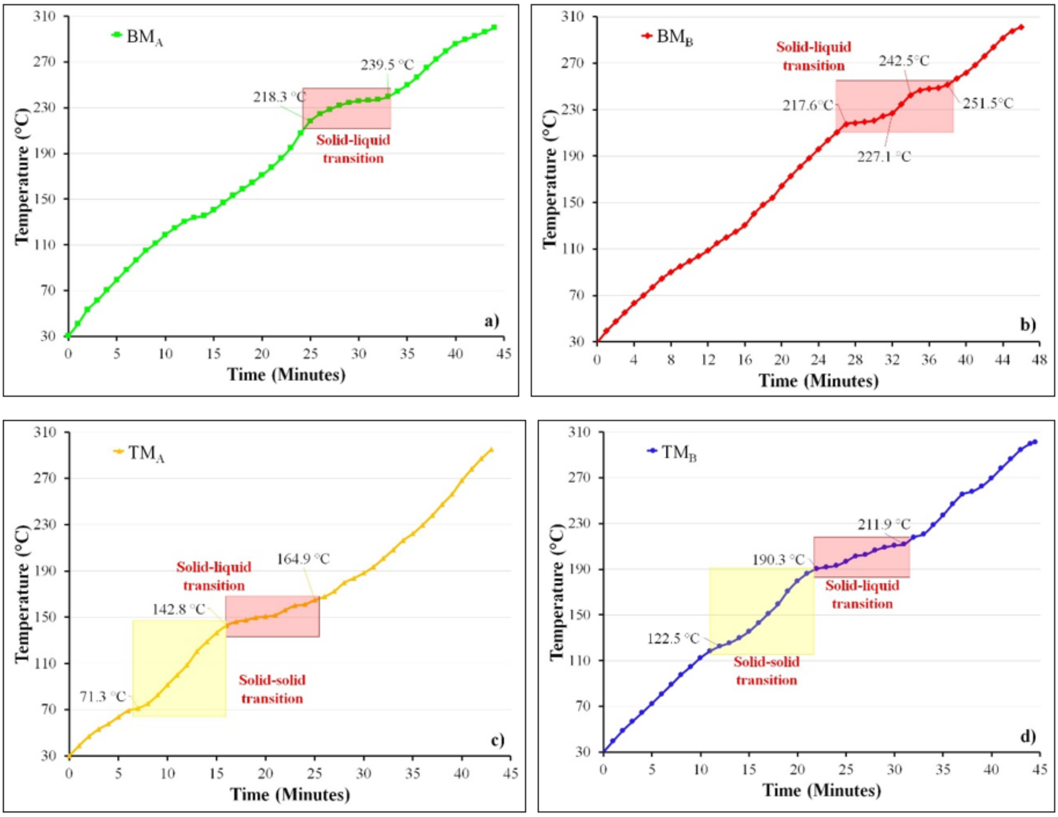

Fig. 3. Temperature evolution profile for each sample.

The heating profile for the binary mixture shows an identic pattern where the phase transition occurs above 200 °C (Fig. 3a and 3b). The slow temperature increment implies partial sensible heating. The heating rate for BMA during phase transition is 3.51 °C/min, whereas BM$_B$ has a relatively lower heating rate (3.08 °C/min). However, the BM$_B$ shows a two-step phase transition, which is undesirable for the LSS tank. Moreover, it has a lower heat of fusion compared to BM$_A$. The high melting temperature for BM$_A$ increases the solid sensible heating. It depends on the heat capacity of the BM$_A$ and probably leads to high-temperature variation for the moderate-temperature LSS tank.

Both ternary mixtures demonstrate solid-solid transition before they reach their phase change region. TM$_A$ starts the solid-solid transition at a relatively lower temperature (71.3 °C, Fig. 3c) than TM$_B$, which starts at 122.5 °C (Fig. 3d). It is affected by the orthorhombic crystalline structure of nitrite. The hygroscopic nature of nitrite also contributes to the phenomenon, which probably leads the water molecules to decompose in the region. It explains that the solid-solid transition starts at a temperature below the boiling point of water. The high melting point of TM$_B$ allows the latent heat to charge at elevated temperatures, similar to the BM$_A$. In this perspective, the TM$_A$ is ideal for medium-temperature LSS tanks since it has a phase transition between 142.8 °C–164.9 °C.

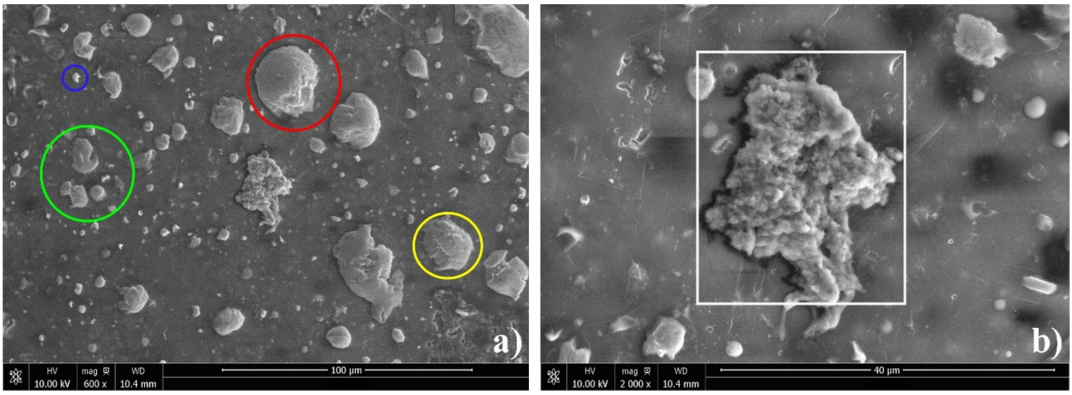

Fig. 4. Temperature evolution profile for each sample.

The scattered profile for TMA demonstrates that each constituent is unmixed adequately due to the nature of the ternary salt mixture. The large particle size (red and yellow circle in Fig. 4a) and the dispersed particle (green and blue circle in Fig. 4a) correspond to each component with different molecular weights. However, one exciting profile is shown in Fig. 4b (white square). It implies that local agglomeration for the salt constituent is possibly affected by aggregation after solidification [36]. It helps ensure a suitable heat transfer rate during charging and discharging for the LSS tank.

Further STP was performed for TM$_A$ (20 g) using different heating rates (Fig. 1). The charging level indicator (CLI) is used according to the heat supplied to the sample for estimating the state of the charge level [37]. The detailed charging profile demonstrates that the solid sensible region occurs distinctively before the phase transition region (Fig. 5a). However, the phase transition region becomes shorter as the heating rate increases. The higher heating rate promotes a shorter phase transition process, allowing the heat to be absorbed instantly. Thus, CLI for TM_A can be rapidly increased, making it suitable for the LSS tank (Fig. 5a).

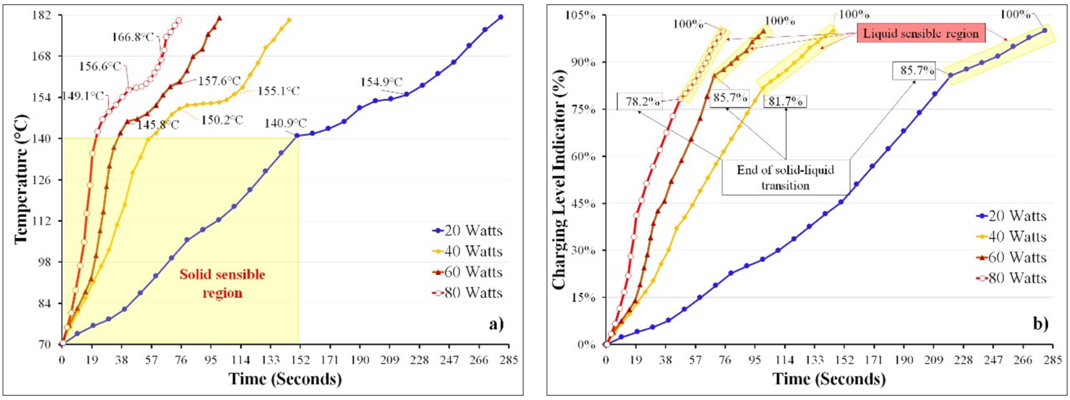

Fig. 5. Temperature and CLI characteristic for TMA under a different charge rate.

The CLI profile (Fig. 5a) demonstrates that the liquid sensible region is less than 20 % of the total capacity. Thus, the effective storage capacity for TM_A can be maintained sufficiently in the LSS tank. The highest specific CLI rate is also suitable for cascaded LSS tanks, which provide a higher storage capacity with a stable outlet temperature [38]. The combined LSS tank with TM_A can be a suitable approach to improve the performance of medium-temperature storage, particularly in the application related to solar renewable sources. The TM_A helps increase the storage temperature with the desirable storage capacity. Thus, the overall performance of a solar thermal system can be increased significantly.

4. CONCLUSION

The medium-temperature LSS tank can be obtained using nitrate-salt as a phase change material (PCM). Four different salts were evaluated and showed high melting temperatures, making them suitable for the LSS tank. The highest melting temperature was obtained for a binary mixture with (60 wt%) potassium nitrate and (40 wt%) sodium nitrate at 223.8 °C. The presence of nitrite (sodium) reduces the heat of fusion by around 35 %–39 %. According to the charge profile, the ternary salt (potassium nitrate/sodium nitrate/sodium nitrite) has the ideal character, which is suitable for the LSS tank. The mixture has a suitable melting transition (142.8 °C–164.9 °C) with an effective CLI of more than 80 %.

The finding of this study provides a fundamental basis for utilising ternary salt as a storage material for medium-temperature LSS tanks. Further research is encouraged by focusing on the stabilized aspect of the salt regarding its phase behaviour. Also, implementing the salt in a specific LSS tank can be taken to analyse the actual heat transfer characteristic using forced convection. Thus, it helps support the design improvement for the storage tank and eventually leads to a higher technology achievement in the solar thermal renewable system.

ACKNOWLEDGEMENTS

The authors are grateful to Universitas Pancasila as being the funder of research under internal grant funding.

REFERENCES

1. Ismail, I., Rahman, R. A., Haryanto, G., & Pane, E. A. (2021). The Optimal Pitch Distance for Maximizing the Power Ratio for Savonius Turbine on Inline Configuration. *International Journal of Renewable Energy Research*, 11 (2), 595–599. https://doi.org/10.20508/ijrer.v11i2.11862.g8181
2. Atalay, H., Yavaş, N., & Turhan Çoban, M. (2022). Sustainability and Performance Analysis of a Solar and Wind Energy Assisted Hybrid Dryer. *Renewable Energy*, *187*, 1173–1183. https://doi.org/10.1016/j.renene.2022.02.020
3. Afzal, A., Iqbal, T., Ikram, K., Anjum, M. N., Umair, M., Azam, M., … & Majeed, F. (2023). Development of a Hybrid Mixed-Mode Solar Dryer for Product Drying. *Heliyon*, *9* (3), e14144. https://doi.org/10.1016/j.heliyon.2023.e14144
4. Kundziņa, A., Geipele, I., Lapuke, S., & Auders, M. (2022). Energy Performance Aspects of Non-Residential Buildings in Latvia. *Latvian Journal of Physics and Technical Sciences*, *59* (6), 30–42. https://doi.org/10.2478/lpts-2022-0045
5. Qiu, S., Ruth, M., & Ghosh, S. (2015). Evacuated Tube Collectors: A Notable Driver behind the Solar Water Heater Industry in China. *Renewable and Sustainable Energy Reviews*, *47*, 580–588. https://doi.org/10.1016/j.rser.2015.03.067
6. Salih, S. M., Jalil, J. M., & Najim, S. E. (2019). Experimental and Numerical Analysis of Double-Pass Solar Air Heater Utilizing Multiple Capsules PCM. *Renewable Energy*, *143*, 1053–1066. https://doi.org/10.1016/j.renene.2019.05.050
7. Abdeldjebar, R., Elmir, M., & Douha, M. (2023). Study of the Performance of a Photovoltaic Solar Panel By Using a Nanofluid as a Cooler. *Latvian Journal of Physics and Technical Sciences*, *60* (3), 69–84. https://doi.org/10.2478/lpts-2023-0018
8. Favakeh, A., Khademi, A., & Shafii, M. B. (2019). Experimental Study of Double Solid Phase Change Material in a Cavity. *7th International Conference On Energy Research and Development, ICERD 2019*, 24–31.
9. Khademi, A., Mehrjardi, S. A. A., Said, Z., & Chamkha, A. J. (2023). Heat Transfer Improvement in a Thermal Energy Storage System Using Auxiliary Fluid Instead of Nano-PCM in an Inclined Enclosure: A Comparative Study. *Journal of Applied and Computational Mechanics*, *9* (2), 475–486. https://doi.org/10.22055/jacm.2022.41867.3829
10. Assari, M. R., Basirat Tabrizi, H., Parvar, M., & Alkasir Farhani, M. (2019). Experimental Investigation Of Sinusoidal Tube in Triplex-Tube Heat Exchanger during Charging and Discharging Processes Using Phase Change Materials. *International Journal of Engineering, Transactions A: Basics*, *32* (7), 999–1009. https://doi.org/10.5829/ije.2019.32.07a.13
11. Kairisa, E., & Mutule, A. (2023). Reliable Data Profiling for Energy Communities - Review of Open-Source Approaches. *Latvian Journal of Physics and Technical Sciences*, *60* (2), 17–30. https://doi.org/10.2478/lpts-2023-0008
12. Suyitno, B. M., Ismail, I., Rahman, R. A. (2023). Improving the performance of a small-scale cascade latent heat storage system by using gradual melting temperature storage tank. *Case Studies in Thermal Engineering*, 45, 103034. https://doi.org/10.1016/j.csite.2023.103034

13. Klimeš, L., Charvát, P., Mastani Joybari, M., Zálešák, M., Haghighat, F., Panchabikesan, K., … & Yuan, Y. (2020). Computer Modelling and Experimental Investigation of Phase Change Hysteresis of PCMs: The State-of-the-Art Review. *Applied Energy*, *263*, 114572. https://doi.org/10.1016/j.apenergy.2020.114572
14. Suyitno, B. M., Pane, E. A., Rahmalina, D., Rahman, R. A. (2023). Improving the operation and thermal response of multiphase coexistence latent storage system using stabilized organic phase change material. *Results in Engineering*, 18, 101210. https://doi.org/10.1016/j.rineng.2023.101210
15. Ma, X., Sheikholeslami, M., Jafaryar, M., Shafee, A., Nguyen-Thoi, T., & Li, Z. (2020). Solidification Inside a Clean Energy Storage Unit Utilizing Phase Change Material with Copper Oxide Nanoparticles. *Journal of Cleaner Production*, *245*, 118888. https://doi.org/10.1016/j.jclepro.2019.118888
16. Putra, N., Rawi, S., Amin, M., Kusrini, E., Kosasih, E. A., & Indra Mahlia, T. M. (2019). Preparation of Beeswax/Multi-Walled Carbon Nanotubes as Novel Shape-Stable Nanocomposite Phase-Change Material for Thermal Energy Storage. *Journal of Energy Storage*, *21*, 32–39. https://doi.org/10.1016/j.est.2018.11.007
17. Elbrashy, A. A., Abou-Taleb, F. S., El-Fakharany, M. K., & Essa, F. A. (2022). Experimental Study of Solar Air Heater Performance by Evacuated Tubes Connected in Series and Loaded with Thermal Storage Material. *Journal of Energy Storage*, *54*, 105266. https://doi.org/10.1016/j.est.2022.105266
18. Ismail, I., Syahbana, M. S. L., & Rahman, R. A. (2022). Thermal Performance Assessment for an Active Latent Heat Storage Tank by Using Various Finned-Coil Heat Exchangers. *International Journal of Heat and Technology*, 40 (6), 1470–1477. https://doi.org/10.18280/ijht.400615
19. Bouselsal, M., Mebarek-Oudina, F., Biswas, N., & Ismail, A. A. I. (2023). Heat Transfer Enhancement Using Al2O3-MWCNT Hybrid-Nanofluid inside a Tube/Shell Heat Exchanger with Different Tube Shapes. *Micromachines*, *14* (1072).
20. Khademi, A., Mehrjardi, S. A. A., Said, Z., Saidur, R., Ushak, S., & Chamkha, A. J. (2023). A Comparative Study of Melting Behavior of Phase Change Material with Direct Fluid Contact and Container Inclination. *Energy Nexus*, *10*, 100196. https://doi.org/10.1016/j.nexus.2023.100196
21. Hosseininaveh, H., Mohammadi, O., Faghiri, S., & Shafii, M. B. (2021). A Comprehensive Study on the Complete Charging-Discharging Cycle of a Phase Change Material Using Intermediate Boiling Fluid to Control Energy Flow. *Journal of Energy Storage*, *35*, 102235. https://doi.org/10.1016/j.est.2021.102235
22. Kulkarni, P., & Muthadhi, A. (2020). Improving Thermal and Mechanical Property of Lightweight Concrete Using n-Butyl Stearate/Expanded Clay Aggregate with Alccofine1203. *International Journal of Engineering, Transactions A: Basics*, *33* (10), 1842–1851. https://doi.org/10.5829/IJE.2020.33.10A.03
23. Orozco, M. A., Acurio, K., Vásquez-Aza, F., Martínez-Gómez, J., & Chico-Proano, A. (2021). Thermal Storage of Nitrate Salts as Phase Change Materials (PCMs). *Materials*, *14* (23). https://doi.org/10.3390/ma14237223
24. Caraballo, A., Galán-Casado, S., Caballero, Á., & Serena, S. (2021). Molten Salts for Sensible Thermal Energy Storage: A Review and an Energy Performance Analysis. *Energies*, *14* (4), 1–15. https://doi.org/10.3390/en14041197
25. Peinado, A., Pliego, A., Pedro, F., & Márquez, G. (2019). A Review of the Application Performances of Concentrated Solar Power Systems. *Applied Energy*, *255*, 113893. https://doi.org/10.1016/j.apenergy.2019.113893
26. Jiang, F., Zhang, L., Cang, D., Ling, X., & Ding, Y. (2021). Preparation and Characterization of a Heat Storage Material: Shape-Stabilized KNO3 Using a Modified Diatomite-Based Porous Ceramic as the Skeleton. *Ceramics International*, *47* (18), 26301–26309. https://doi.org/10.1016/j.ceramint.2021.06.040
27. Dunlop, T. O., Jarvis, D. J., Voice, W. E., & Sullivan, J. H. (2018). Stabilization of Molten Salt Materials Using Metal Chlorides for Solar Thermal Storage. *Scientific Reports*, *8* (1), 1–7. https://doi.org/10.1038/s41598-018-26537-8

28. Lincu, D., Ioniţă, S., Mocioiu, O. C., Berger, D., Matei, C., & Mitran, R. A. (2022). Aluminum Doping of Mesoporous Silica as a Promising Strategy for Increasing the Energy Storage of Shape Stabilized Phase Change Materials Containing Molten NaNO3: KNO3 Eutectic Mixture. *Journal of Energy Storage*, *49*. https://doi.org/10.1016/j.est.2022.104188
29. Qu, Y., Wang, S., Tian, Y., & Zhou, D. (2019). Comprehensive Evaluation of Paraffin-HDPE Shape Stabilized PCM with Hybrid Carbon Nano-Additives. *Applied Thermal Engineering*, *163*. https://doi.org/10.1016/j.applthermaleng.2019.114404
30. Favakeh, A., Khademi, A., & Shafii, M. B. (2023). Experimental Investigation of the Melting Process of Immiscible Binary Phase Change Materials. *Heat Transfer Engineering*, *44* (2), 154–174. https://doi.org/10.1080/01457632.2022.2034085
31. Cárdenas-Ramírez, C., Jaramillo, F., Fernández, A. G., Cabeza, L. F., & Gómez, M. A. (2021). Influence of Thermal Treatments on the Absorption and Thermal Properties of a Clay Mineral Support Used for Shape-Stabilization of Fatty Acids. *Journal of Energy Storage*, *36*. https://doi.org/10.1016/j.est.2021.102427
32. Lu, Y., Zhang, G., Hao, J., Ren, Z., Deng, Z., Xu, G., … & Chang, L. (2019). Fabrication and Characterization of the Novel Shape-Stabilized Composite PCMs of Na2CO3-K2CO3/MgO/Glass. *Solar Energy*, *189*, 228–234. https://doi.org/10.1016/j.solener.2019.07.064
33. Mitran, R. A., Lincu, D., Buhălţeanu, L., Berger, D., & Matei, C. (2020). Shape-Stabilized Phase Change Materials Using Molten NaNO3 – KNO3 Eutectic and Mesoporous Silica Matrices. *Solar Energy Materials and Solar Cells*, *215*. https://doi.org/10.1016/j.solmat.2020.110644
34. Jančík, P., Schmirler, M., Hyhlík, T., Bláha, A., Sláma, P., Devera, J., & Kouba, J. (2021). Experimental Investigation and Modelling of a Laboratory-Scale Latent Heat Storage with Cylindrical PCM Capsules. *Scientific Reports*, *11* (1), 1–15. https://doi.org/10.1038/s41598-021-02705-1
35. Fernández, A. G., Galleguillos, H., Fuentealba, E., & Pérez, F. J. (2015). Thermal Characterization of HITEC Molten Salt for Energy Storage in Solar Linear Concentrated Technology. *Journal of Thermal Analysis and Calorimetry*, *122* (1), 3–9. https://doi.org/10.1007/s10973-015-4715-9
36. Jiang, F., Zhang, L., She, X., Li, C., Cang, D., Liu, X., … & Ding, Y. (2020). Skeleton Materials for Shape-Stabilization of High Temperature Salts Based Phase Change Materials: A Critical Review. *Renewable and Sustainable Energy Reviews*, *119*, 109539. https://doi.org/10.1016/j.rser.2019.109539
37. Zsembinszki, G., Orozco, C., Gasia, J., Barz, T., Emhofer, J., & Cabeza, L. F. (2020). Evaluation of the State of Charge of a Solid/Liquid Phase Change Material in a Thermal Energy Storage Tank. *Energies*, *13* (6). https://doi.org/10.3390/en13061425
38. Li, P., Xu, C., Liao, Z., Ju, X., & Ye, F. (2020). Numerical Investigation on the Thermal Performance of a Cascaded Latent Heat Thermal Energy Storage. *Frontiers in Heat and Mass Transfer*, *15* (1), 1–10. https://doi.org/10.5098/hmt.15.10
39. Mayilvelnathan, V., & Valan Arasu, A. (2020). Experimental Investigation on Thermal Behavior of Graphene Dispersed Erythritol PCM in a Shell and Helical Tube Latent Energy Storage System. *International Journal of Thermal Sciences*, *155*, 106446. https://doi.org/10.1016/j.ijthermalsci.2020.106446
40. Barz, T., & Emhofer, J. (2021). Paraffins as Phase Change Material in a Compact Plate-Fin Heat Exchanger - Part I: Experimental Analysis and Modeling of Complete Phase Transitions. *Journal of Energy Storage*, *33*. https://doi.org/10.1016/j.est.2020.102164
41. Janghel, D., Saha, S. K., & Karagadde, S. (2020). Effect of Shrinkage Void on Thermal Performance of Pure and Binary Phase Change Materials Based Thermal Energy Storage System: A Semi-analytical Approach. *Applied Thermal Engineering*, *167*, 114706. https://doi.org/10.1016/j.applthermaleng.2019.114706

LATVIAN JOURNAL OF PHYSICS
AND TECHNICAL SCIENCES
2024, N 1

DOI: 10.2478/lpts-2024-0007

GENERAL AND COMPLETE SYNCHRONIZATION OF MUTUAL COUPLING SYSTEM OF QUANTUM DOT SEMICONDUCTOR LASERS WITH OPTICAL FEEDBACK

O. H. Abdulkareem [1], R. H. AbdAli *[2],
B. A. Ghalib [1]

[1] Department of Laser Physics,
Science College for Women, Babylon University,
Al Hillah, Babylon Governorate, IRAQ
[2] Physics Department, Science College,
University of Karbala,
Karbala – Hilla Rd, Karbala 56001, IRAQ
*e-mail: rajaa.ali@uokerbala.edu.iq

The study examines an extensive and complete synchronization of optimal feedback with quantum dot semiconductor laser mutual coupling system. This has been achieved by resolving the transmitter and receiver equations of the quantum dot lasers. Numerous crisis areas have been observed at the time of investigating the relationship between photon density and time. The authors have selected an optimal time delay for the optical feedback so as to render an appropriate situation for intermittent dynamics. The study analyses the impact created by a long external cavity of QDSL upon the synchronization process in this mutual coupling system, in the presence of the enhancement factor of (α =3).

Keywords: *Crisis route, linewidth enhancement factor, nonlinear dynamics, optical feedback, quantum dot, semiconductor laser.*

1. INTRODUCTION

In a private communication domain, in order to keep the chaos among varying types of dynamical systems under control, the researchers have started to give preference to a chaotic synchronization process in recent years [1]. Thus, the most investigated research topic is synchronization phenomena under Quantum Dot (QD) laser chaotic. This is attributed to the sensitive nature of the phenomenon against external perturbation as an optimal feedback. Such materials execute discrete transition of the energy in addition to the predicted symmetric emission lines. These materials possess a low linewidth enhancement factor. Such a concept has been extensively investigated due to its multi-faceted applications, especially the removal of laser [2].

One of the vibrant phenomena that is discussed in different domains of physical sciences is crisis-induced intermittency. It is characterised by the unannounced creation of inappropriate bursts, out of regular evolution, under a varying number of control parameters. Such a dynamic system is managed by changing two dynamics that correspond to intermittent evolutions on two distant sub-attractors (attractor expansion) or two co-existing attractors (attractor merging) [3].

The size of QDs is in the range of a few nanometres (2–10 nm), and these minuscule-level semiconductor particles contain both electron and the holes across the spatial dimensions [4]. On the other hand, such minimal-sized QDs possess excellent optical and electronic characteristics that are unique compared to that of the large-sized particles. Pecora and Carroll proposed the concept of chaos synchronization between two nonlinear systems. These researchers utilised Lorenz system and three variables to demonstrate the proposed model [5]. The Quantum Dot Semiconductor Laser (QDSL) possesses three primary characteristics such as low threshold current density, small linewidth enhancement factor (LEF) and high characteristic temperature [6]. This synchronization setup is called complete chaos synchronization that is distinct compared to the generalization synchronization of chaotic oscillations [7]. In telecommunication applications, the QD nanostructures are generally utilised thanks to confinement of the carrier within three dimensions [8], [9]. In general, the carrier dynamics is believed to create a crucial and a negative impact on the outcomes of QD laser under optimal feedback [10] and optical injection [11].

In comparison with the rest of the SLs, the QDSLs show high sensitivity to any sort of changes in the time delay, when used with optoelectronic feedback circuits [12]. Complete and generalized chaos synchronization are two different origins of the chaos synchronization process in nonlinear delay differential systems. In the generalized chaos synchronization, soon after the transmitter signal is received, a synchronized wave form is produced by the receiver. Thus, there is a time lag between the outputs. In case of complete chaos synchronization, at the receiver, the asynchronous chaotic signal is produced before receiving the transmitter signal. For comparison, the time lag in complete chaos synchronization is lesser than that of the signal transmission that occurs between the transmitter and receiver systems [13].

2. RATE EQUATION OF QUANTUM DOT LASER

In a rate equations method, three coupled equations are included, such as the carrier density (N), photon density (E) and occupation probability (ρ). In case of QD semiconductor devices, the wetting layer is first injected with the carriers prior to its inculcation into dots at a capture rate that is severely based on the population of the dots. Equations (1)–(3) correspond to the rate equations [14], [15]. Thus, the rate equations generally denote the carrier dynamics of QD materials [16]:

$$\frac{dE_{(T,R)}}{dt}=E_{(T,R)}\left(-\frac{1}{2t_s}+\frac{g_o\upsilon}{2}(2\rho_{(T,R)}-1)\right)+\frac{\gamma}{2}E_{(T,R)}(t-\tau_{(T,R)})+\frac{\gamma}{2}E_{(T,R)}(t-\tau_c)+R_{sp} \quad (1)$$

$$\frac{d\rho_{(T,R)}}{dt}=-t_n\,\rho_{(T,R)}-g_o(2\rho_{(T,R)}-1)\left|E_{(T,R)}\right|^2+CN_{(T,R)}^2(1-\rho_{(T,R)}) \quad (2)$$

$$\frac{dN_{(T,R)}}{dt}=J_{(T,R)}-\frac{N_{(T,R)}}{t_d}-2n_d\,CN_{(T,R)}^2(1-\rho_{(T,R)}) \quad (3)$$

Here, $N_{(T,R)}$ denotes the carrier density in the well for both transmitter and the receiver lasers, $E_{(T,R)}$ corresponds to the complex amplitude of the electric field for both transmitter and receiver lasers, the occupation probability in a dot is denoted by $\rho_{(T,R)}$ for a transmitter laser and a receiver laser, the lifetime of the photon is denoted by t_s; t_n and *td* correspond to the timelines of the carrier in well and dot, respectively; n_d denotes the 2D density of the dots; and finally the pump is denoted by $J_{(T,R)}$. γ and $\tau_{T,R}$ denote the feedback level and delay time correspondingly for the transmitter laser and the receiver laser. Here, $\tau = 2L/c$ corresponds to the round-trip time of light within the external cavity (L) and *c* denotes the velocity of light [15]. *C* corresponds to Auger carrier capture rate [16].

The researchers conducted the theoretical investigation of the mutual coupling system which might possess either one type or both types of synchronization, for instance, complete and generalized for transmitter and receiver quantum dot semiconductor lasers with optical feedback. The same laser value exists for both on linewidth enhancement factor (=3), current density whereas it is different in case of coupling time delay between the transmitter and receiver lasers, τ_c.

3. RESULTS AND DISCUSSION

MATLAB software was used to simulate the values for photon density, occupation probability, carrier number and the attractor with the help of 4th order Runge-Kutta numerical method. Figure 1a portrays the QDSL photon density as a function of time when $\alpha = 3$, ($\tau = 124\,ps$). The density of the photon reached 32*10^{20} m^{-2} and also diminished to a chaotic behaviour. There was no periodic behaviour observed for the transmitter and receiver of the QDSL, whereas the attractor between the photon density values of the receiver and transmitter lasers was clearly not periodic with non-synchronization as shown in Fig. 1b. Figure 1c, e shows the time series for the photon density values of the transmitter and receiver (of QDSL) lasers, when $\alpha = 3$, ($\tau = 125\ \mathit{and}\ 126\ \mathit{ps}$). Thus, there is stability in the behaviour at a steady state period. General and complete synchronization outcomes are shown in Fig. 1d, f, while from Fig. 1a, c, e, it can be understood that the change on time delay by 1 ps is a good outcome to be applied further.

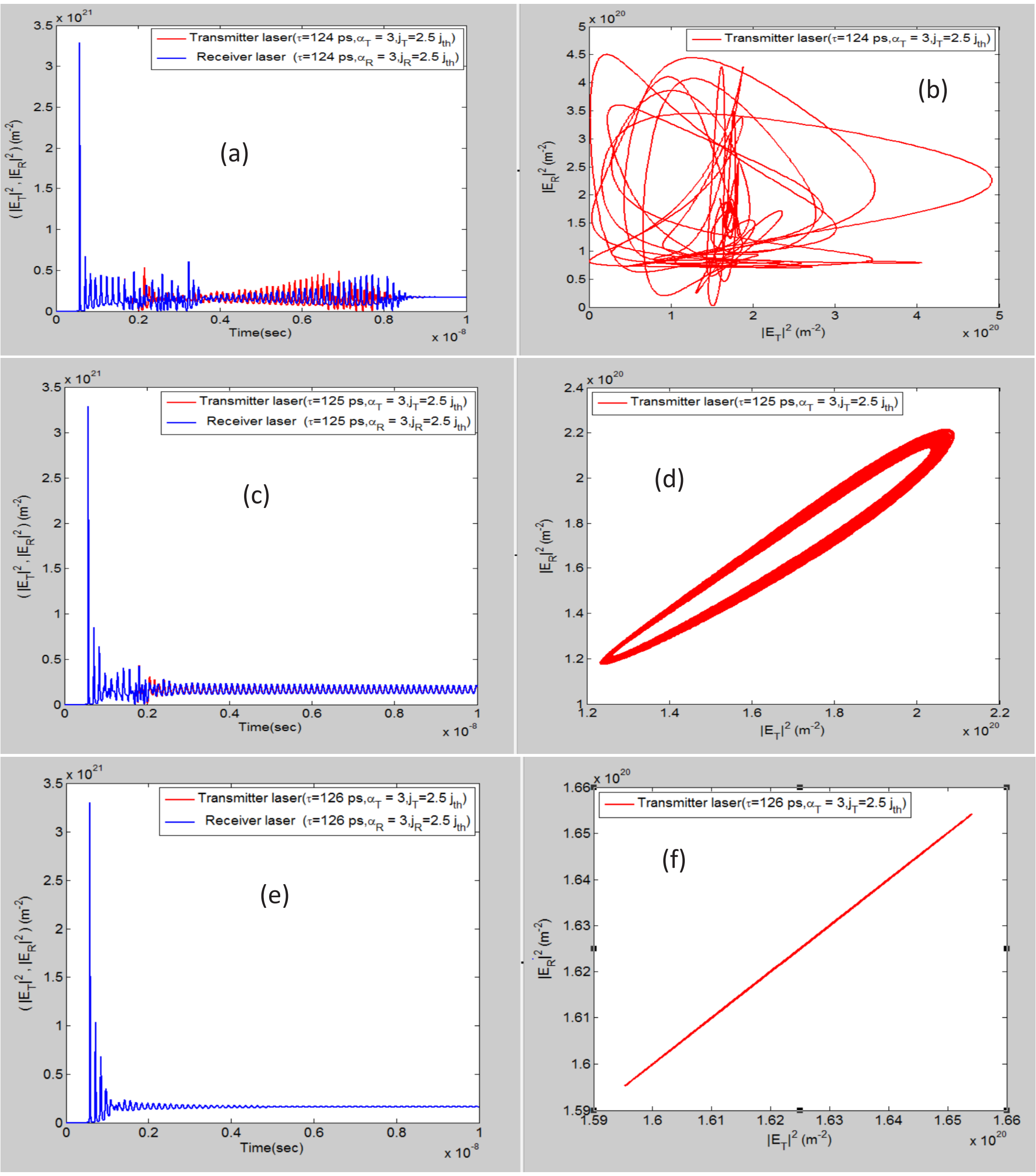

Fig. 1. Photon density of transmitter and receiver (QDSL) as a function of time at various values of time delay as in (a, c, e) chaotic attractor and stable for photon density of transmitter as a function of photon density of receiver (QDSL); (b) chaotic; (d) general synchronization; (f) complete synchronization.

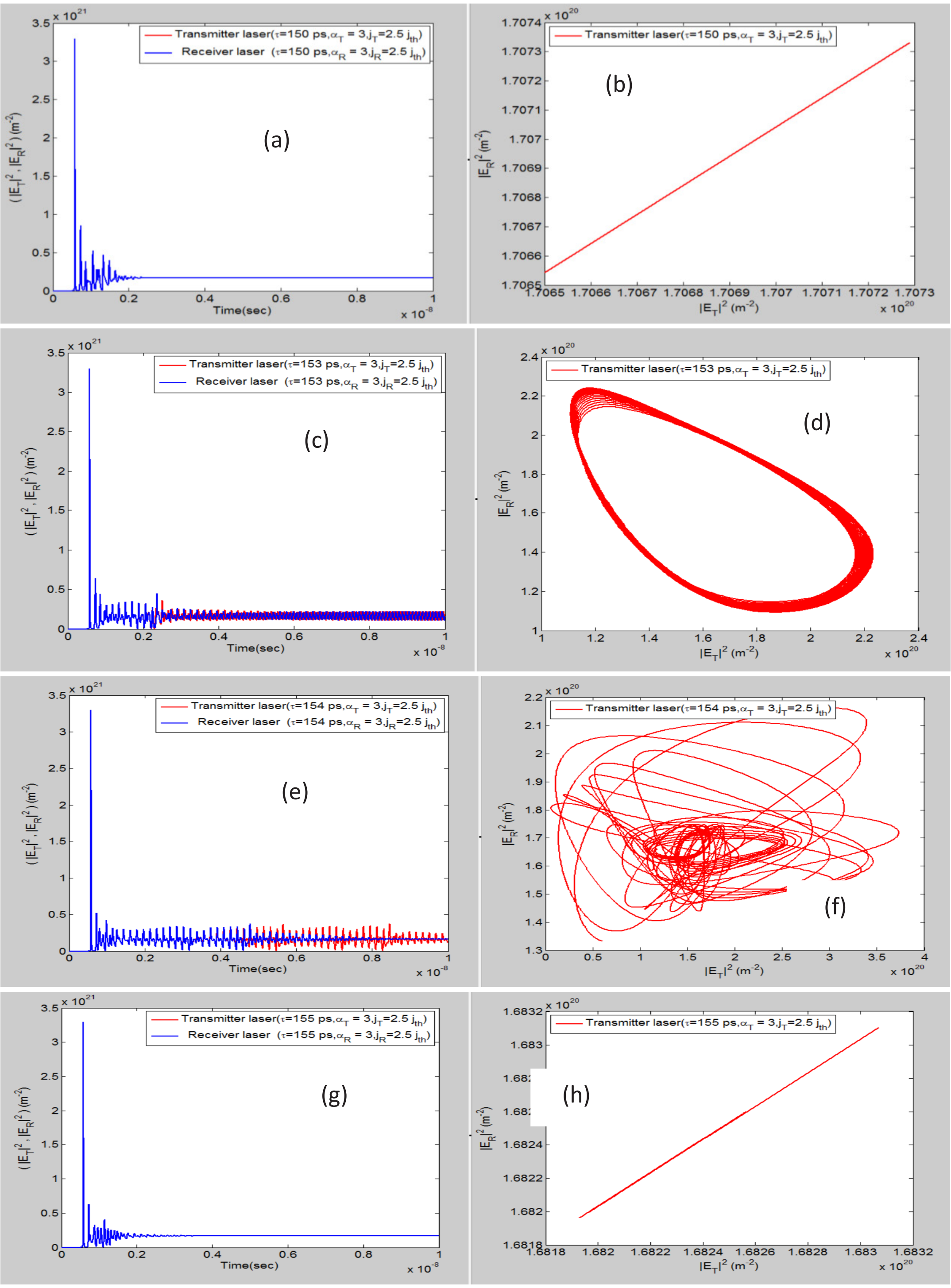

Fig. 2. Photon density of transmitter and receiver (QDSL) as a function of time for various values of time delay as in (c, e) chaotic attractor; (a, g) stable; (b, h) complete attractor synchronization; (d) general attractor synchronization; (f) chaotic behaviour for photon density of transmitter as a function of photon density of receiver (QDSL).

Figure 2a portrays the photon density values of the QDSL as a function of time, when $\alpha = 3$, ($\tau = 150ps$). According to the figure, the photon density values attained $32*10^{20}$ m^{-2}, whereas the stable behaviour of the QDSL transmitter and receiver along with complete synchronization is shown in Fig. 2b. The researchers found a clear chaotic behaviour of the photon density of both receiver and transmitter lasers in case of general synchronization between the photon density of the receiver and transmitter lasers as in Fig. 2c, d, when ($\tau = 153ps$). Further, Figs. 2e and 2f show an excellent chaotic behaviour for transmitter and receiver lasers of the QDSL and attractor with non-synchronization between the photon density of the receiver laser and the respective transmitter laser, when ($\tau = 154ps$). Due to the complete synchronization at ($\tau = 155ps$), the outcomes were good to be used on applications with a stable behaviour as shown in Fig. 2g, h.

The photon density of QDSL, as a function of time, when $\alpha = 3$, is($\tau = 395, 400, 410, 415, 420\, ps$) respectively (see Fig. 3a, c, e, g, i). The chaotic behaviour is demonstrates in case of the whole existing values and the photon density of $18*10^{20}$ m^{-2}. Figures 3f and 3j show a stable behaviour of the transmitter and receiver lasers of the QDSL with complete synchronization. The intermediate chaotic behaviours of the photon density of receiver and transmitter lasers between the complete and general synchronization are illustrated in Fig. 3b, d and h. The chaos synchronization between the photon density of the receiver and transmitter lasers is shown, when ($\tau = 395, 400, 415\, ps$).Figures 3f and 3j portray an excellent chaotic behaviour for transmitter and receiver of the QDSL and attractor with synchronization between the photon density of the receiver laser and the transmitter laser. These outcomes are crucial in the development of communication applications.

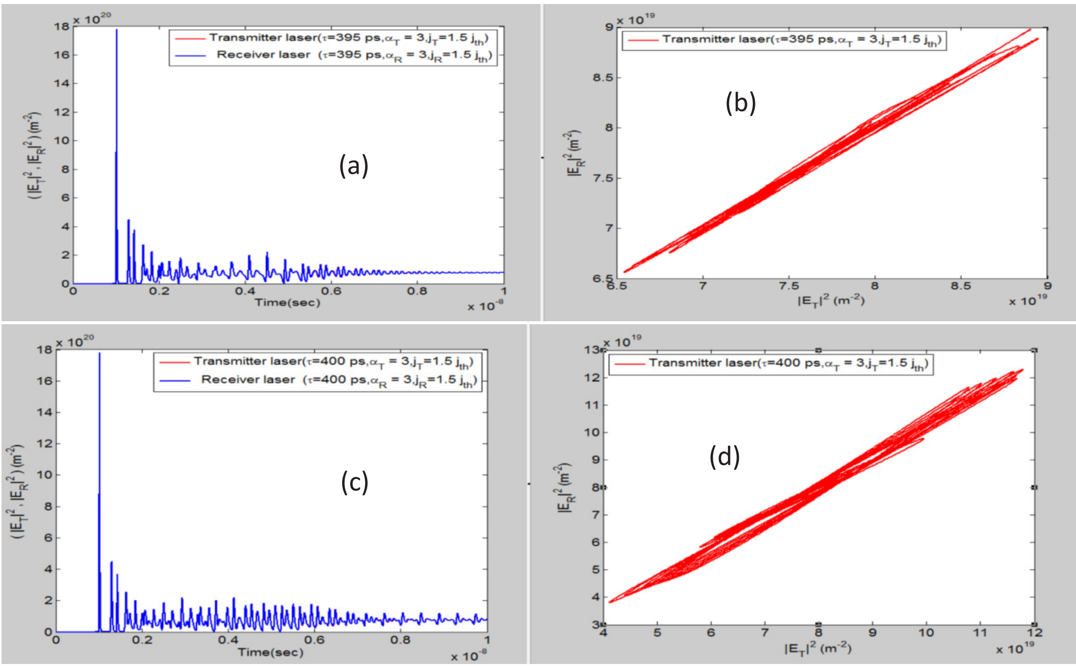

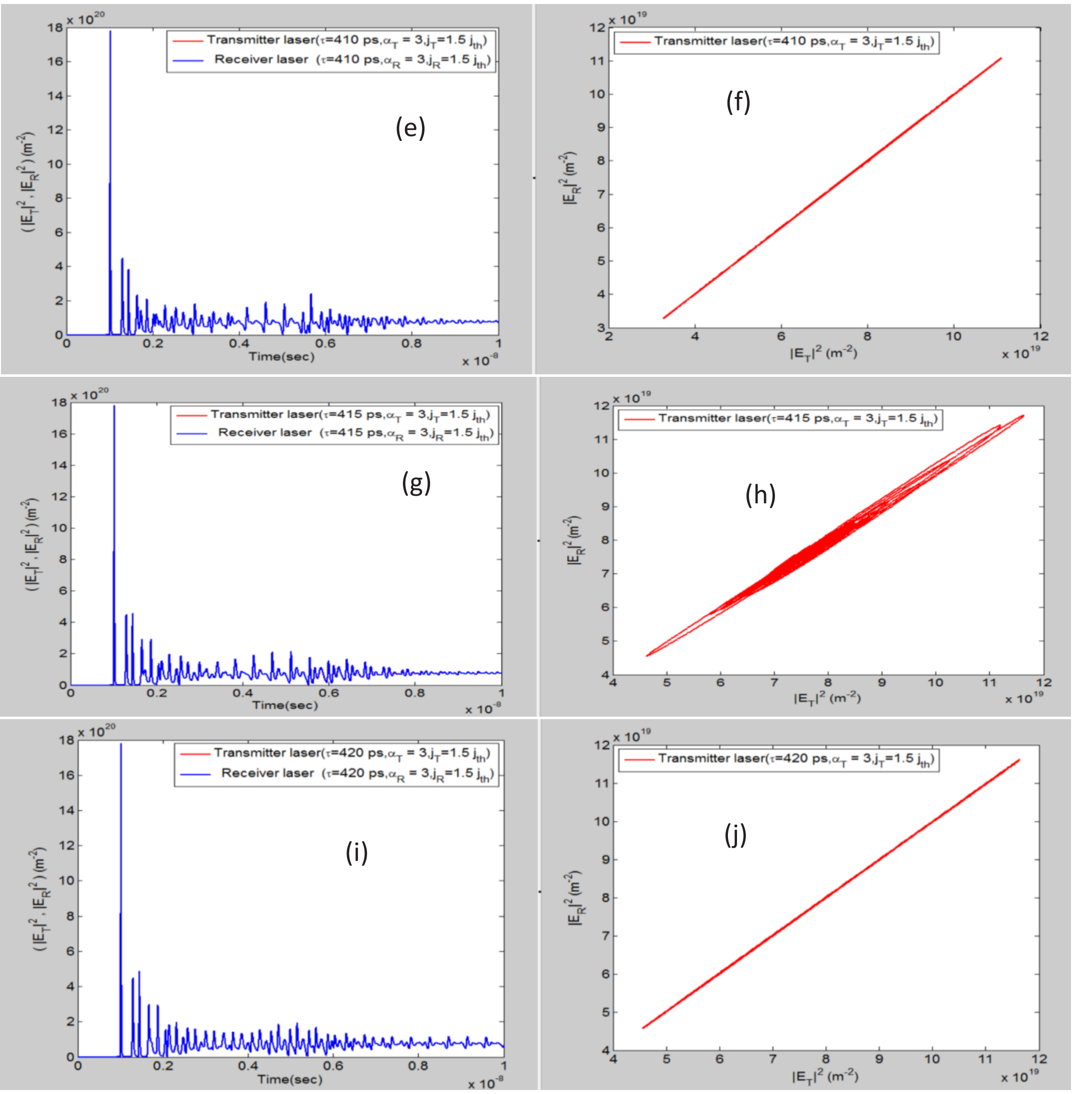

Fig. 3. Photon density of transmitter and receiver (QDSL) as a function of time for various values of time delay as in (a, c, e, g, i) chaotic; (b, d, f) like complete attractor synchronization; (h, j) complete synchronization of QDSL.

CONCLUSIONS

The authors of the current study conducted generalized and complete synchronization of the QDSL mutual coupling system along with optical feedback, on the basis of time delay. The impact of the QDSL with optical feedback dynamics, under a linewidth enhancement factor of 3, remains an important behaviour in the chaotic synchronization process. The study reached excellent outcomes at (τ = 410, 420 *ps*) with complete synchronization that could be applied in coding and decoding signal communication activities.

REFERENCES

1. Al Husseini, H. B. (2016). Control of Nonlinear Dynamics of Quantum Dot Laser with External Optical Feedback. *Journal of Nanotechnology in Diagnosis and Treatment, 4*, 5–14.
2. Al Husseini, H. B., Al Naimee, K. A., Al-Khursan, A. H., & Khedir, A.H. (2016). External Modes in Quantum Dot Light Emitting Diode with Filtered Optical Feedback. *Journal of Applied Physics 119* (22), 224301.
3. Gouhei, T., Sanjuan, M.A.F., & Aihara, K. (2005). Crisis-Induced Intermittency in Two Coupled Chaotic Maps: Towards Understanding Chaotic Itinerancy. *Physical Review E* 71, *1*, 016219.
4. Demchenko, A. P. (2008). *Introduction to Fluorescence Sensing*. Springer Science & Business Media.
5. Pecora, L. M., & Carroll, T.L. (1990). Synchronization in Chaotic Systems. *Physical Review Letters, 64* (8), 821.
6. Al-Husseini, H., Al-Khursan, A. H., & Al-Dabagh, S. Y. (2009). III-Nitride QD Lasers. *The Open Nanoscience Journal, 3* (1), 1–11.
7. Al-Khursan, A. H., Ghalib, B. A., & Al-Obaidi, S. J. (2012). Numerical Simulation of Optical Feedback on a Quantum Dot Lasers. *Semiconductors, 46* (2), 213–220.
8. Huyet, G., O'Brien, D., Hegarty, S. P., McInerney, J. G., Uskov, A. V., Bimberg, D., ... & White, J. K. (2004). Quantum Dot Semiconductor Lasers with Optical Feedback. *Physica Status Solidi (a), 201* (2), 345–352.
9. Viktorov, E. A., Mandel, P., & Huyet, G. (2007). Long-Cavity Quantum Dot Laser. *Optics Letters,* 32 (10), 1268–1270.
10. Ohtsubo, J. (2002). Chaos Synchronization and Chaotic Signal Masking in Semiconductor Lasers with Optical Feedback. *IEEE Journal of Quantum Electronics, 38* (9), 1141–1154.
11. Ghalib, B. A., Al-Obaidi, S. J., & Al-Khursan, A. H. (2013). Carrier Scenarios in Optically Injected Quantum-Dot Semiconductor Lasers. *Optics Communications, 308*, 243–247.
12. Ghalib, B. A., Al-Obaidi, S. J., & Al-Khursan, A. H. (2013). Modeling of Synchronization in Quantum Dot Semiconductor Lasers. *Optics & Laser Technology, 48*, 453–460.
13. Ghalib, B. A., Al-Obaidi, S. J., & Al-Khursan, A. H. (2012). Quantum Dot Semiconductor Laser with Optoelectronic Feedback. *Superlattices and Microstructures, 52* (5), 977–986.
14. Sugawara, M., Mukai, K., & Shoji, H. (1997). Effect of Phonon Bottleneck on Quantum-Dot Laser Performance. *Applied Physics Letters, 71* (19), 2791–2793.
15. Uskov, A. V., Boucher, Y., Le Bihan, J., & McInerney, J. (1998). Theory of a Self-Assembled Quantum-Dot Semiconductor Laser with Auger Carrier Capture: Quantum Efficiency and Nonlinear Gain. *Applied Physics Letters, 73* (11), 1499–1501.
16. O'Brien, D., Hegarty, S. P., Huyet, G., & Uskov, A. V. (2004). Sensitivity of Quantum-Dot Semiconductor Lasers to Optical Feedback. *Optics letters, 29* (10), 1072–1074.
17. Tromborg, B., Osmundsen, J., & Olesen, H. (1984). Stability Analysis for a Semiconductor Laser in an External Cavity. *IEEE Journal of Quantum Electronics, 20* (9), 1023–1032.
18. Rajesh, S., & Nandakumaran, V. M. (2006). Control of Bistability in a Directly Modulated Semiconductor Laser Using Delayed Optoelectronic Feedback. *Physica D: Nonlinear Phenomena, 213* (1), 113–120.
19. Dal Bosco, A. K., Akizawa, Y.., Kanno, K., Uchida, A., Harayama, T., & Yoshimura, K. (2016). Photonic Integrated Circuits Unveil Crisis-Induced Intermittency. *Optics Express, 24* (19), 22198–22209.